

# Performance of graphene Hall effect sensors: role of bias current, disorder and Fermi velocity

Lionel Petit<sup>1</sup>, Tom Fournier<sup>1,2</sup>, Géraldine Ballon<sup>1</sup>, Cédric Robert<sup>1</sup>, Delphine Lagarde<sup>1</sup>, Pascal Puech<sup>2</sup>, Thomas Blon<sup>1</sup> and Benjamin Lassagne<sup>1</sup>

<sup>1</sup> Université de Toulouse, INSA-CNRS-UPS, LPCNO, 135 Av. Ranguel, 31077 Toulouse, France

<sup>2</sup> Centre d'Elaboration des Matériaux et d'Etudes Structurales (CEMES), UPR8011 CNRS, Université Toulouse 3, 31055 Toulouse, France

E-mail: lassagne@insa-toulouse.fr

Graphene Hall effect magnetic field sensors hold great promise for the development of ultra-sensitive magnetometers. Their performance is frequently analysed using the two-channel model where electron and hole conductivities are simply added. Unfortunately, this model is unable to capture all the features of the sensor, particularly the bias current dependence of the magnetic field sensitivity. Here we present an advanced model that provides an in-depth understanding of how graphene Hall sensors operate, and demonstrate its ability to quantitatively assess their performance. First, we report the fabrication of sensors with different qualities of graphene, with the best devices achieving magnetic field sensitivities as high as 5000 ohms/T, outperforming the best silicon and narrow-gap semiconductor-based sensors. Then, we examine their performance in detail using the proposed numerical model, which combines Boltzmann formalism, with distinct Fermi levels for electrons and holes, and a new method for the introduction of substrate-induced electron-hole puddles. Importantly, the dependences of magnetic field sensitivity on bias current, disorder, substrate and Hall bar geometry are quantitatively reproduced for the first time. In addition, the model emphasizes that the performance of devices with widths of the order of the charge carrier diffusion length, is significantly affected by the bias current due to the occurrence of large and non-symmetric carrier accumulation and depletion areas near the edges of the Hall bar. The formation of these areas induces a transverse diffusion particle flux capable of counterbalancing the particle flux induced by the Lorentz force when the Hall electric field cancels out in the ambipolar regime. Finally, we discuss how sensor performance can be enhanced by Fermi velocity engineering, paving the way for future ultra-sensitive graphene Hall effect sensors.

**Keywords:** Graphene, Graphene Hall sensor, magnetic field sensor, Hall effect, Boltzmann formalism, Fermi velocity renormalization, electron-hole puddles

## I. INTRODUCTION

The market for magnetic field sensors is currently very large, with applications in a wide range of fields such as automotive, consumer electronics, position and motion sensing, magnetic storage, magnetic field mapping, biosensing, or fundamental research on magnetic [1] or superconducting [2] materials. The most used magnetic field sensor technology is based on the measurement of the well-known transverse Hall voltage  $U_h$  which appears in a thin, long bar-shaped conductive material, supplied with a bias current  $I$  and immersed in a perpendicular magnetic field  $B$  [3]. The success of Hall effect sensors is based on this very simple and nonperturbative measurement scheme, combined with a linear response over a wide range of magnetic fields and temperatures [3–5], unlike superconducting quantum interference devices [6] or magnetoresistive sensors based on giant and tunnel magnetoresistance effect [6], which are limited to cryogenic temperatures and low magnetic fields, respectively.

New directions for the development of Hall sensors were made possible by the discovery of graphene in 2004 [7]. With intrinsic one-atom thick structure, very high charge carrier mobility [8] and low charge carrier density, graphene Hall sensors (GHS) show an unprecedented magnetic field sensitivity ( $S_I = U_h/(B \times I)$ ) and outperform state-of-the-art silicon and narrow-gap semiconductor Hall sensors [4,6,9–13]. As a result, GHS have been demonstrated as either ultrasensitive magnetic field sensors for magnetometry [14,15] and nanoscale magnetic field mapping [13] or sensors having Hall voltages of the same order of magnitude as those obtained with silicon sensors

but with 100 times lower power consumption [6]. This latter point represents a significant advance and paves the way for the development of ultra-low power devices.

The trend toward ever-improving sensor performance requires a thorough understanding of the physical principles that govern their operation. In the case of GHS, the Hall effect is frequently analysed through the so-called two-channel model [4,11,16,17] which intrinsically possesses limitations in the capture of all the GHS reported features. In particular, the bias current dependence of  $S_I$  observed in several previous works [6,11,17–19] cannot be explained since the two-channel model equations were obtained for an electrodeless Hall bar with uniform charge carrier doping and infinite length. In this paper, we analyse the Hall effect in GHS of different quality and size fabricated with graphene grown by chemical vapor deposition (CVD) or graphene exfoliated from a crystal of highly orientated pyrolytic graphite (HOPG) using a more advanced physical model combining several approaches. The charge carrier transport properties are described through the Boltzmann formalism, where electrons and holes are treated with distinct Fermi levels in contrast to the two-channel model. A local field effect model is used to account for the effect of gate and bias current on electron and hole doping, and a new semi-empirical model of electron and hole puddles is developed to account for the effect of impurities. As a result, we can quantitatively describe for the first time all the GHS galvanomagnetic features. In particular, we highlight and explain how the bias current affects the spatial profile of the electron and hole doping inside the GHS, resulting in a significant modification of the shape of  $S_I$  as a function of gate voltage and bias current especially for devices having a width comparable to the charge carrier diffusion length. This later point, which is related to the graphene ambipolar nature has never been addressed before. Also, we shed light on the role of electron-hole puddles and substrates on  $S_I$ , revealing thus a new way to improve GHS performance by engineering the graphene Fermi velocity.

## II. EXPERIMENTAL RESULTS

### A. Electrical characteristics of Hall bars

GHS were fabricated either from CVD graphene monolayers (from Graphenea) transferred using a semi-dry technique onto  $90 \pm 10 \text{ nm}$  thick  $\text{SiO}_2/\text{Si}$  doped substrates (referred as CVD-GHS in the following) or HOPG graphene monolayers (from HQ Graphene) deposited by mechanical exfoliation onto  $285 \pm 10 \text{ nm}$  thick  $\text{SiO}_2/\text{Si}$  heavily doped substrates (referred as HOPG-GHS in the following) or by encapsulation of a HOPG graphene monolayer in hexagonal boron nitride (h-BN, from HQ Graphene) using a pick-up technique [20], and transferred onto  $285 \pm 10 \text{ nm}$  thick  $\text{SiO}_2/\text{Si}$  heavily doped substrates (referred as hBN-GHS in the following). Polymethylmethacrylate masks, typically 8-branches Hall bars, defined through e-beam lithography were used to etch the graphene with successive  $\text{SF}_6$  and  $\text{O}_2$  plasma, the former one being used only for hBN-GHS. Electrodes were then patterned by e-beam lithography followed by Cr/Au (5 nm/25 nm for HOPG and hBN-GHS and 5 nm/200 nm for CVD-GHS) Joule heating evaporation. The typical GHS width/length dimensions are  $5 \mu\text{m}/60 \mu\text{m}$ ,  $1 \mu\text{m}/17 \mu\text{m}$  and  $2 \mu\text{m}/11 \mu\text{m}$  for CVD, HOPG and hBN-GHS, respectively. Finally, electrical measurements were performed under vacuum in a physical property measurement system under magnetic field at 0.1 T and 1 T. CVD-GHS were measured at 200 K to avoid hysteresis on the gate voltage while HOPG and hBN-GHS, for which there is no hysteresis, were measured at 300 K.

Several samples of each kind (CVD-GHS, HOPG-GHS and hBN-GHS) were fabricated, their characteristics were highly reproducible. Figures 1(a)-(f) show typical Raman spectra and optical images of our devices. The Raman spectra (Figs. 1(a)-1(c)) display G ( $\approx 1580 \text{ cm}^{-1}$ ) and 2D peaks ( $\approx 2680 \text{ cm}^{-1}$ ) with ratios  $I_{2D}/I_G \approx 2.41$ ,  $I_{2D}/I_G \approx 2.82$  and  $I_{2D}/I_G \approx 3.9$  for CVD-GHS, HOPG-GHS and hBN-GHS respectively, confirming that our devices are made of monolayer graphene [21]. Note that the presence of the D ( $1342 \text{ cm}^{-1}$ ) and D' ( $1623 \text{ cm}^{-1}$ ) peaks on the Fig. 1(a) is characteristic of monolayers containing impurities and grain boundaries obtained by CVD. Figures 1(g)-1(l) show typical compensated longitudinal resistance  $R_{LC} = (R_L(B) + R_L(-B))/2$  and typical compensated magnetic field sensitivity  $S_{IC} = (S_I(B) + S_I(-B))/2$  for different bias current values. We observe the expected shapes for  $R_{LC}$  and  $S_{IC}$  [4,6,10–12] with a maximum  $S_{IC}$  reaching  $5000 \Omega/T$  for hBN-GHS (black line on Fig. 1(l)), a value identical to the best report to date on similar structures [10]. Moreover, on the Figs. 1(j)-1(l), we observe a pronounced effect of the bias current on the shape of  $S_{IC}$  as previously reported in similar devices [6,11,17–19]. The gate voltage position of the charge neutrality point (CNP), where  $S_{IC}$  inverts, shifts towards positive voltages as the current increases, resulting, in the case of CVD-GHS, in a quasi-rigid translation of  $S_{IC}$  as a function of  $V_g$ . For HOPG and hBN-GHS, the increase in bias current also leads to a CNP

shift but accompanied with a drop of the maximum  $|S_{IC}|$  as well as an increase in the distance separating  $S_{IC}$  extrema. This effect is very significant for the hBN-GHS resulting in a large shape  $S_{IC}$  modification as previously reported by Shaeffer et al [6].

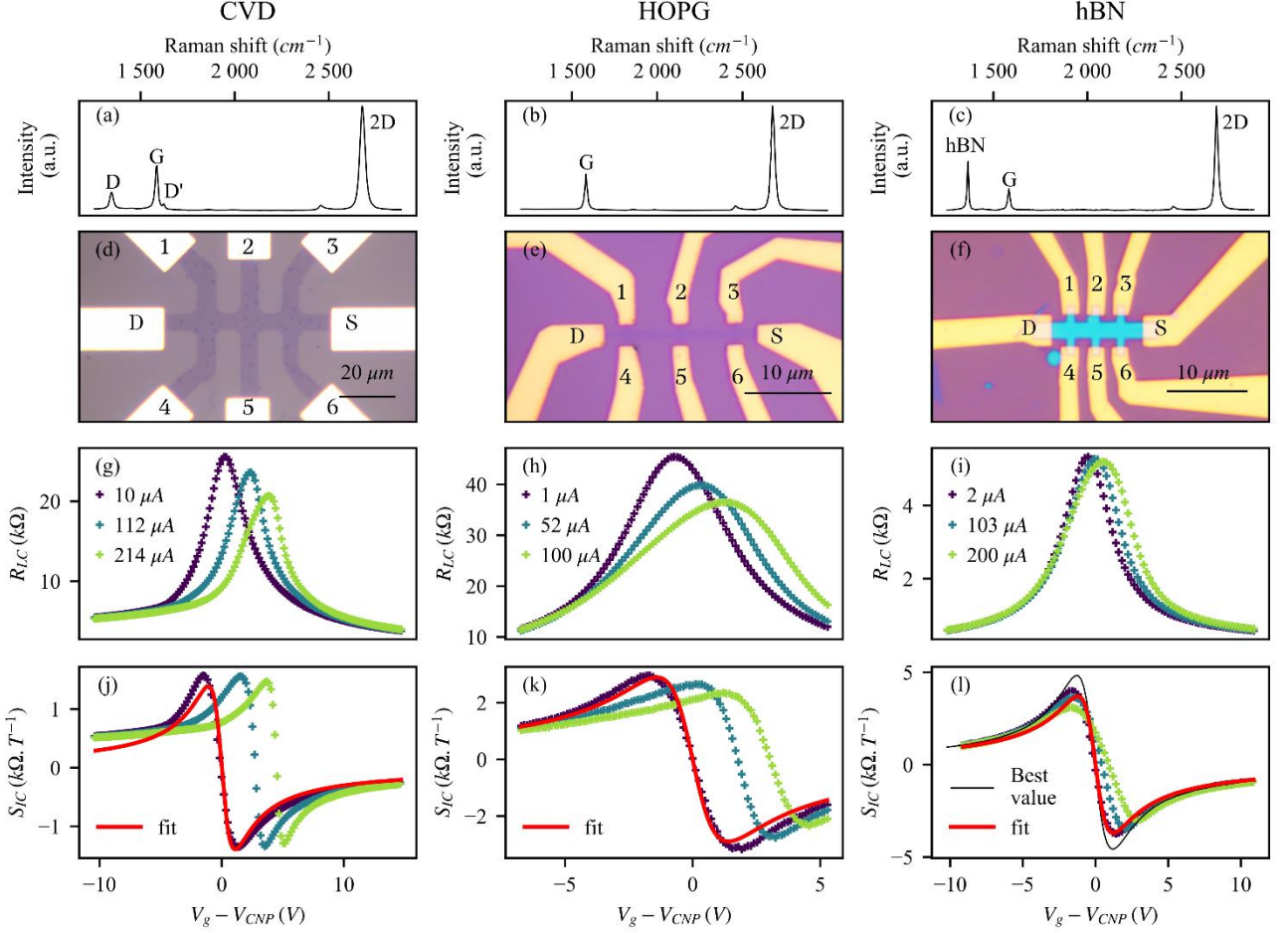


FIG. 1. Typical Raman spectra of CVD-GHS (a), HOPG-GHS (b) and hBN-GHS (c). Typical optical images of CVD-GHS (d), HOPG-GHS (e) and hBN-GHS (f). (g), (h) and (i) Typical compensated longitudinal 4 probe resistance  $R_{LC}$  measured between contacts 1 and 3 as a function of gate voltage  $V_g$  and for different bias current values. ((g) 200 K, 1 T,  $V_{CNP} = 5.32$  V ; (h) 300 K, 0.1 T,  $V_{CNP} = 7.73$  V ; (i) 300 K, 0.1 T,  $V_{CNP} = -2.88$  V). (j), (k) and (l) Typical compensated magnetic field sensitivity  $S_{IC}$  as a function of  $V_g$  for different bias current values (measured between contacts 1 and 4 for (j) and (k) and 2 and 5 for (l), same  $T$  and  $B$  values as for  $R_{LC}$ ). The red line curves are the fit of the low-bias current  $S_{IC}$  using Eq. 1 and 2 and obtained with the following fit parameters: (j)  $t_{ox} = 105$  nm,  $n_0 = 2.24 \times 10^{11}$  cm $^{-2}$ , (k)  $t_{ox} = 280$  nm and  $n_0 = 1.08 \times 10^{11}$  cm $^{-2}$  and (l)  $t_{ox} = 310$  nm and  $n_0 = 8.5 \times 10^{10}$  cm $^{-2}$ .

## B. Analysis with the two-channel model

In a first step, we analysed  $S_I$  at low bias current using the two-channel model, as previously reported [4,11,16,17]. This model gives a fairly simple expression for  $S_I$  when the charge carrier mobility  $\mu_n$  and  $\mu_p$  are equal and  $\mu_{n(p)}B \ll 1$ ,

$$S_I = -\frac{1}{e} \frac{(n-p)}{(n+p)^2} \quad (1)$$

With  $e$ , the elementary charge,  $n$  and  $p$  the electron and hole densities. The gate voltage dependence of  $S_I$  is taken into account using empirical relationships established by Meric et al [22]

$$n + p \approx \sqrt{n_0^2 + n(V_g)^2} \quad (2a)$$

$$n - p = n(V_g) = \frac{C_g}{e} (V_g - V_{CNP}) \quad (2b)$$

with  $n_0$  the minimal carrier doping as determined by temperature and residual impurities,  $C_g$  the gate capacitance per surface unit,  $V_g$  the gate voltage and  $V_{CNP}$  the gate voltage at CNP. The red line curves on the Figs. 1(j)-(l) are the fits of the experimental data using Eqs. 1 and 2. The oxide thicknesses  $t_{ox}$  were determined from the gate capacitance values and equal to 105 nm, 280 nm, and 310 nm for the CVD, HOPG and hBN-GHS respectively. Regarding the residual doping  $n_0$ , we obtained values of  $2.24 \times 10^{11} \text{cm}^{-2}$ ,  $1.08 \times 10^{11} \text{cm}^{-2}$  and  $8.5 \times 10^{10} \text{cm}^{-2}$  for CVD, HOPG, and hBN-GHS respectively, which is consistent with the fact that CVD graphene monolayers have more defects and the h-BN encapsulation protects graphene from charged impurities and process contamination. Equations 1 and 2 are quite convenient for an initial analysis of  $S_I$  at low bias current as it allows both to understand the effect of the doping on the GHS sensitivity and to extract important parameters such as the residual doping value or the gate capacitance. Unfortunately, this approach remains limited, particularly for anticipating the device geometry and bias current effects on  $S_I$ . Therefore, further developments require an advanced model that should consider the exact GHS geometry as well as the influence of the gate voltage and bias current on the carrier doping spatial distribution.

### III. ADVANCED MODEL

The model we developed is based on the combination of several approaches used to describe the graphene transport properties in the diffusive regime. Thermal carrier doping and transport properties are described using the Boltzmann formalism and electrostatic doping is taken into account thanks to a field effect model, as has been done previously for graphene field effect transistors [22–25]. In the present work, some refinements have been made. Distinct electron and hole Fermi levels have been used and recombination-generation processes have been added to describe more precisely the operation of the GHS in the ambipolar regime. We have also developed a new method to take account of the presence of impurities.

#### A. Carrier thermal statistics and electric charge

The temperature dependence of the electron and hole doping  $n$  and  $p$  is taken into account by the following expressions

$$n(E_{fn}) = \int_{E_{CNP}}^{\infty} f_n(E) D(E) dE \quad (3a)$$

$$p(E_{fp}) = \int_{-\infty}^{E_{CNP}} (1 - f_p(E)) D(E) dE \quad (3b)$$

where  $D(E) = 2|E - E_{CNP}|/\pi(\hbar v_f)^2$  is the graphene density of states,  $E$  the electron energy for a state with a wave vector  $\vec{k}$ ,  $E_{CNP}$  the energy at the CNP,  $\hbar$  the reduced Plank constant and  $v_f$  the Fermi velocity.  $f_n(E)$  and  $f_p(E)$  are the Fermi-Dirac distribution of the electrons and holes given by  $f_{n(p)}(E) = 1/(1 + \exp((E - E_{fn(p)})/k_B T))$  with  $k_B$  the Boltzmann's constant,  $T$  the temperature and  $E_{fn(p)}$  the electron (hole) Fermi level. We also define the shift of the Fermi level  $\Delta E_{fn(p)}$  as follows  $\Delta E_{fn(p)} = E_{fn(p)} - E_{CNP}$  (Fig. 2(b)).

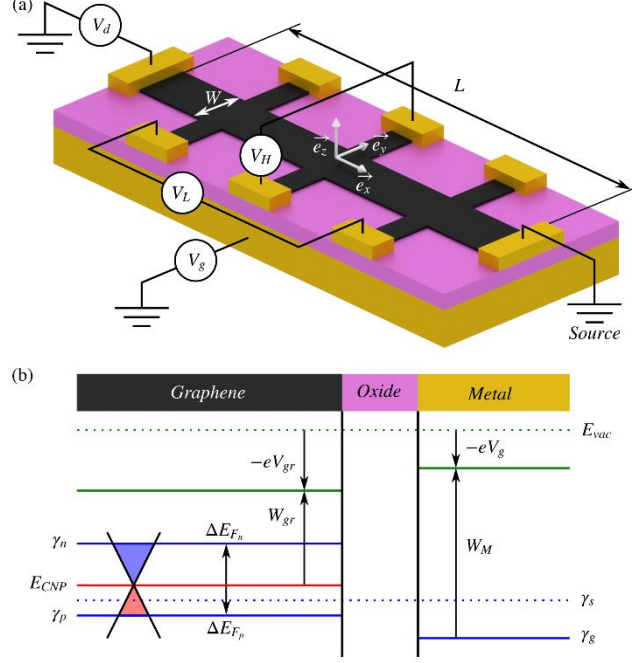


FIG. 2. (a) Typical device geometry.  $V_D$  is the drain electrostatic potential, the source is the reference electrostatic potential set to zero. (b) Band diagram of the graphene and gate electrode.  $E_{vac}$  corresponds to the electron energy in vacuum.

Regarding the effect of the gate voltage and bias current on the electron and hole doping in graphene, we used a field effect model [22–25]. In this framework, the source is used as the reference electrostatic potential. Its Fermi level represents the origin of the energy, thus its electrochemical potential  $\gamma_S$  is equal to 0 eV and the electrochemical potential  $\gamma_D$  of the drain electrode, with tuneable electrostatic potential  $V_D$ , is equal to  $-eV_D$  (Fig. 2(a)). For the sake of simplicity, the doped silicon substrate which serves as the back-gate electrode is modelled by a metallic electrode (Fig. 2(a)) having an electrochemical potential  $\gamma_g$  equal to  $-eV_g$  (Fig. 2(b)). Finally, the electrochemical potentials  $\gamma_n$  and  $\gamma_p$  of the electrons and holes in graphene are defined by  $\gamma_{n(p)} = E_{fn(p)} - eV_{gr}$  with  $V_{gr}$  the electrostatic potential in graphene (Fig. 2(b)). The graphene CNP energy (red line in Fig. 2(b)) is defined as  $E_{CNP} = W_M - W_{gr} - eV_{gr}$ , with  $W_M$  and  $W_{gr}$  the metal and graphene work function. Then, using Gauss's law [24-26], a simple and local relationship between  $V_g$ ,  $V_{gr}$  and the charge carrier density in the graphene sheet  $Q_{gr} = -e(n(\gamma_n + eV_{gr}) - p(\gamma_p + eV_{gr}))$  can be found

$$Q_{gr}(x, y) + Q_g(x, y) + Q_0(x, y) = 0 \quad (4)$$

With  $Q_g = C_g(V_g - V_{gr})$  the local electric charge density in the gate electrode and  $Q_0$  a possible residual electric charge density coming from contamination and impurities. For the sake of simplicity, we will consider in the following  $W_M = W_{gr}$ , and use  $Q_0$  to simulate the work function difference between metallic electrodes and graphene.

## B. Transport properties

To describe the galvanomagnetic properties of GHS in a perpendicular magnetic field (along  $z$ , Fig. 2(a)) we used the Boltzmann formalism [3,23]. The electric current density  $\vec{J}$  in graphene is the sum of the contribution of the electrons,  $\vec{J}_n$  and holes,  $\vec{J}_p$ , i.e  $\vec{J} = \vec{J}_n + \vec{J}_p$  with

$$\vec{J}_{n(p)} = \bar{\sigma}_{n(p)} \frac{\vec{\nabla} \gamma_{n(p)}}{e} \quad (5)$$

$\bar{\sigma}_{n(p)}$  is the antisymmetric conductivity tensor for electrons (holes). Its components  $\sigma_{xxn(p)}$  and  $\sigma_{xy_{n(p)}}$  are given by,

$$\sigma_{xxn(p)} = \frac{\eta e}{\pi v_f^2 \hbar^2} \int_{E_{CNP}}^{-\eta \times \infty} \frac{(E - E_{CNP})^2 \mu(E)}{1 + \mu^2(E) B^2} \frac{\partial f_{n(p)}}{\partial E} dE \quad (6a)$$

$$\sigma_{xy_{n(p)}} = \frac{eB}{\pi v_f^2 \hbar^2} \int_{E_{CNP}}^{-\eta \times \infty} \frac{(E - E_{CNP})^2 \mu^2(E)}{1 + \mu^2(E) B^2} \frac{\partial f_{n(p)}}{\partial E} dE \quad (6b)$$

with  $\eta = -1$  for electrons and  $\eta = 1$  for holes. The charge carrier mobility  $\mu(E)$  depends on the charge carrier scattering mechanisms (charged impurities, vacancies, ripples, phonons...) [26,27] and is expressed in terms of the scattering time  $\tau_i$  of each mechanism by  $\mu(E) = ev_f^2 |E - E_{CNP}|^{-1} (\sum_i 1/\tau_i(E))^{-1}$ . Equations 5 and 6, where the electrochemical potentials are considered unequal for electrons and holes, allow for both conduction and diffusion currents. The latter can have a significant contribution when a  $p$ - $n$  junction forms in the GHS [23] or when charge carriers accumulate and deplete near the edges of the Hall bar, especially in the ambipolar regime [28] (see Sec. IV).

In this work we focus on the stationary regime, hence conservation of electric charge implies that the divergences of electron and hole current densities are given by

$$\vec{\nabla} \cdot \vec{J}_{n(p)} = -\eta e R = -\eta e k (np - n_{eq} p_{eq}) \quad (7)$$

$R$  is the recombination-generation rate of the carriers. Different processes can participate in the electron-hole pair recombination-generation such as Auger scattering, optical and acoustic phonon scattering, or impurity assisted scattering [29,30] but the use of the exact  $R$  expression is beyond the scope of this article. Instead, we use a linear expression (see Eq. 7) characterized by a constant  $k$ , specific of the recombination-generation process and by  $n_{eq}$  and  $p_{eq}$  the electron and hole doping at the equilibrium. This latter expression gives a fairly good account of the dependence of the recombination-generation rate on electron and hole doping for a small deviation from equilibrium. Finally,  $\gamma_n$ ,  $\gamma_p$  and  $V_{gr}$ , the solutions of the coupled Eqs. 4, 5 and 7, are obtained using the finite-element method with appropriate geometry and boundary conditions.

### C. Electron-hole puddle model

Electron-hole puddles in graphene have been observed experimentally by scanning tunnelling microscopy (STM) [31,32]. They originate from charged impurities in the substrate and/or fabrication process contamination [26], and possibly from graphene sheet deformation [33]. These electron-hole puddles play an important role in the electronic transport properties of graphene, introducing long-range type charge carrier scattering and residual charge carrier doping which lead to a non-universal minimum conductivity [26,27,34].

To account for this effect, we developed a semi-empirical method to generate maps of random electron-hole puddles that was guided by experimental observations [31,32,35], theoretical calculations based on the Thomas-Fermi-Dirac formalism [36] and empirical modelling [22,37]. The method consists in generating maps of random Fermi level fluctuations  $\Delta E_{fr}$  by adding a given density  $n_{ol}$  of Lorentzian like function  $L_i(x, y) = \left(1 + \frac{\|O_i \vec{M}\|^2}{r_{0i}^2}\right)^{-1/2}$  with  $x, y$ , the  $M$  coordinates,  $r_{0i}$  a random radius and  $O_i(x_{oi}, y_{oi})$ , a random position. The map of  $\Delta E_{fr}$  was calculated using the following ansatz

$$\Delta E_{fr}(x, y) = \Delta E_{frmax} \tanh \left( \sum_{i=1}^{n_{ol}} L_i(x, y) \right) \quad (8)$$

where  $\Delta E_{frmax}$  is the maximum amplitude of the fluctuations of the Fermi level. As explained by E. Rossi et al [36] who developed an effective medium theory to study the electronic transport in disordered graphene, the puddles that primarily contribute to the charge carrier transport concern wide regions spanning the system size, presenting a low carrier density and an almost uniform conductivity. Equation 8 is well adapted to generate such wide charge carrier puddles (Fig. 10(a)) and to reproduce qualitatively Fermi level fluctuations observed experimentally [31,32,35]. Finally, to include the effect of electron-hole puddles in the model presented previously, the map of random Fermi level fluctuations is converted into a map of random gate voltage fluctuations  $\Delta V_g(x, y)$  (see Supplemental material [38] Sec. I, Eq. s1) and added to the Eq. 4 through the electric charge density in the gate as follows  $Q_g(x, y) = C_g(V_g + \Delta V_g(x, y) - V_{gr}(x, y))$ .

#### IV. RESULTS OF THE ADVANCED MODEL

In this part, we report the main findings of the physical model presented in Sec. III. First an in-depth comparison with the two-channel model highlights what new physical mechanisms our advanced model brings, then a focus is made on how the puddles, bias current and geometry affect  $R_L$  and  $S_I$ . For all the explanations given in the following, the simulations were performed on 8-branches Hall bars of width  $W$ , electrode width  $W_h = W/i_h$ , total transversal length  $W' = i' \times W$  with  $i_h$  and  $i'$  positive integers, and total longitudinal length  $L = 8W + 3W_h$  (Fig. 2(a)), allowing to keep the aspect ratio and then, the resistance, constant when varying  $W$ . Each branch of the Hall bar was connected to a metallic electrode of length  $W/2$  with a constant conductivity  $\sigma_c = 1 \text{ S}$  corresponding to a 25 nm thick gold film. For the sake of simplicity,  $Q_0$  was set to zero, the main effect of this parameter is to shift the CNP gate position. We fixed  $\gamma_n = \gamma_p = \gamma_D$  at the drain electrode and  $\gamma_n = \gamma_p = 0$  at the source electrode. Moreover, we imposed  $\gamma_n = \gamma_p$  on the boundaries between graphene and metallic electrodes in order to keep them equal inside the electrodes. The Hall voltage was defined as  $-eU_h = \gamma_{n(p)}(0, -W'/2) - \gamma_{n(p)}(0, W'/2)$  and the longitudinal 4-probe voltage as  $-eU_L = \gamma_{n(p)}(-2W - W_h, W'/2) - \gamma_{n(p)}(2W + W_h, W'/2)$  (Fig. 2(a)). In the simulations presented below, we used the following parameters:  $v_f = 10^6 \text{ m/s}$ ,  $B = 100 \text{ mT}$ ,  $T = 300 \text{ K}$  and  $C_g = 1.15 \text{ F/m}^2$  corresponding to an oxide thickness  $t_{ox}$  of 300 nm. Regarding  $k$ , we used a value equal to  $10^{-4} \text{ m}^2/\text{s}$  corresponding to recombination times  $\tau_r \approx 1/k(n_{eq} + p_{eq})$  ranging from 1 ps to 10 ps depending on the doping (see Supplemental material [38] Sec. II, Eq. s7). These values were in agreement with theoretical predictions at room temperature for pristine graphene [29,30]. The scattering of charge carriers were considered to come from long range disorder which means the charge carrier mobility  $\mu$  is constant and equal for electrons and holes [26,27]. Regarding  $n_{eq}$  and  $p_{eq}$ , they were determined considering that electrons and holes have the same Fermi level  $E_{Feq}$  and that the equilibrium electric charge  $Q_{eq}(E_{feq}) = -e(n_{eq}(E_{feq}) - p_{eq}(E_{feq}))$  is equal to  $Q_{gr}(E_{fn}, E_{fp})$ .

##### A. Comparison with the two-channel model

A major difference between our advanced model and the two-channel model is that the electron and hole currents are calculated using different electrochemical potentials in the former case and only the electrostatic potential for the latter, meaning the electric current densities are simply written in the two-channel model as following  $\vec{J}_{n(p)} = -\bar{\sigma}_{n(p)} \vec{\nabla} V_{gr}$ . To understand why the two-channel model is not sufficient to capture correctly the operation of a GHS, we need to consider not only the electric charge and associated electric current densities but also the carrier densities and associated fluxes  $\vec{P}_{n(p)} = \eta \vec{J}_{n(p)}/e$ . At low bias current and low magnetic field, the total transverse electric current density  $J_y$  and total carrier flux  $P_y$  write in the two-channel model (see Supplemental material [38] Sec.II, Eqs. s2 and s3)

$$J_y = -e(n - p)\mu^2 B \frac{\partial V_{gr}}{\partial x} - e(n + p)\mu \frac{\partial V_{gr}}{\partial y} \quad (9a)$$

$$P_y = (n + p)\mu^2 B \frac{\partial V_{gr}}{\partial x} + (n - p)\mu \frac{\partial V_{gr}}{\partial y} \quad (9b)$$

Equations 9(a) and 9(b) reveal why the two-channel model is inconsistent in describing the GHS operation, in particular at the CNP, when  $n = p$  and the electric charge on the Hall bar edges is null. Indeed, even if  $J_y$  is nullified by the removal of the transverse electric field  $\partial V_{gr}/\partial y$  due to the absence of electric charge and the equality of  $n$  and  $p$ ,  $P_y$  is not and writes  $P_y = 2n\mu^2 B \times \partial V_{gr}/\partial x$ . It is inconsistent for a finite structure. This contribution to the carrier flux is caused by the Lorentz force, which deflects both types of carriers in the same transverse direction [28], normally leading to an excess of carriers near one edge and a deficit on the opposite one, consistent with a zero electric charge. This issue is not taken into account by the two-channel model which is focused on the electric charge and not the carrier densities. It can be solved by the introduction of different electrochemical potentials for electrons and holes allowing their accumulation or depletion near the edges. In our advanced model, the total transverse electric current density  $J_y$  and total carrier flux  $P_y$  write as follow (see Supplemental material [38] Sec. II, Eqs. s4 and s5)

$$J_y = -e(n - p)\mu^2 B \frac{\partial V_{gr}}{\partial x} + \mu \left( n \frac{\partial E_{fn}}{\partial y} + p \frac{\partial E_{fp}}{\partial y} \right) - e(n + p)\mu \frac{\partial V_{gr}}{\partial y} \quad (10a)$$

$$P_y = (n + p)\mu^2 B \frac{\partial V_{gr}}{\partial x} - \frac{\mu}{e} \left( n \frac{\partial E_{fn}}{\partial y} - p \frac{\partial E_{fp}}{\partial y} \right) + (n - p)\mu \frac{\partial V_{gr}}{\partial y} \quad (10b)$$

As seen with Eq. 9(b) the first term of Eq. 10(b) is caused by the Lorentz force (noted  $P_{yL}$  in the following), the second term, which depends on the transverse gradient of the Fermi levels ( $\partial E_{fn}/\partial y$ ,  $\partial E_{fp}/\partial y$ ) is a transverse diffusion flux induced by the accumulation and depletion of carriers near the edges of the Hall bar (noted  $P_{yD}$  in the following), and the third term is simply the Hall electric field term (noted  $P_{yH}$  in the following). At the CNP, where  $n = p$ , as seen previously,  $P_{yH}$  cancels and only  $P_{yD}$  can counterbalance  $P_{yL}$ , solving the inconsistency of the two-channel model. We can also note that when  $n = p$ ,  $\partial E_{fp}/\partial y = -\partial E_{fn}/\partial y$ , ensuring that the electric current density also cancels.

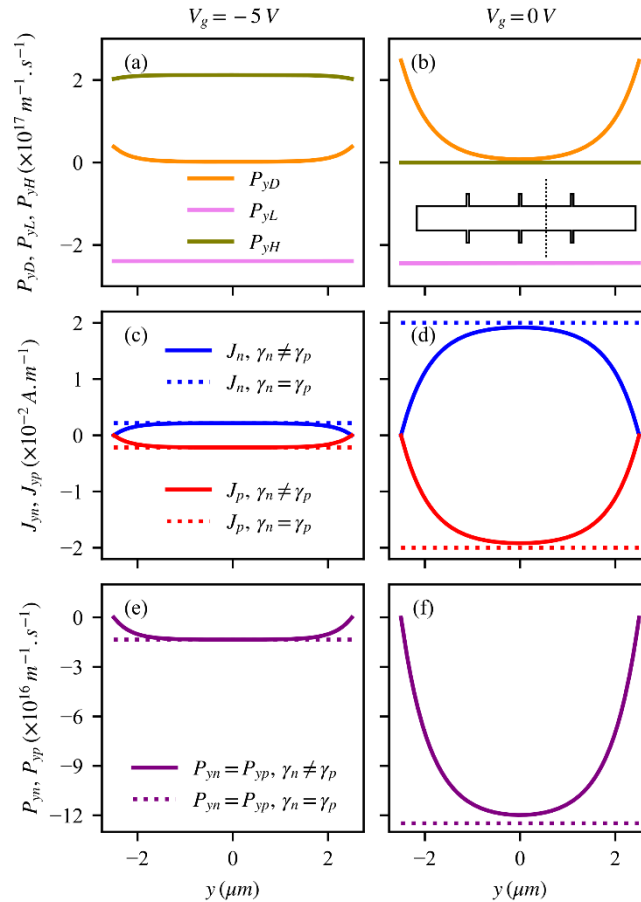




FIG. 3. (a) and (b) Different contributions of  $P_y$  for two  $V_g$  along one transverse cut of the Hall bar (see insert in (b)).  $P_{yL}$  is the Lorentz component,  $P_{yD}$ , the diffusion component and  $P_{yH}$  the Hall component. Electron and hole current densities (c) and (d) and carrier fluxes (e) and (f) for two  $V_g$  calculated with our model (solid line) and in the case  $\gamma_n = \gamma_p = \gamma$  (dotted lines).

To illustrate the above discussion, simulations were performed at low bias current,  $1 \mu A$  on a Hall bar having a  $\mu = 2 \text{ m}^2/(V.s)$  and a width  $W = 5 \mu m$ . We used  $W' = 2W$  and  $W_h = W/10$  to ease the comparison with the two-channel model which was established for an electrodeless Hall bar. Figures 3(a)-3(b) show the different contributions of  $P_y$  for two gate voltages ( $V_g = -5 \text{ V}$  and  $V_g = 0 \text{ V}$ ) along one transverse cut of the Hall bar (see the insert in Fig. 3(b)). We can note that the shape of the different contributions of  $P_y$  are almost uniforms along the  $x$  direction (see Supplemental material [38] Sec. II, Fig. S1). When one kind of carrier dominates the doping (hole, at  $V_g = -5 \text{ V}$ ),  $P_{yL}$  is principally counterbalanced by  $P_{yH}$  while at the CNP ( $V_g = 0 \text{ V}$ ), only  $P_{yD}$  counterbalances  $P_{yL}$ . We observe that the total carrier flux is rigorously null at the edges while it is not in the central part of the Hall bar. Figures 3(c)-3(f) show the transverse electron and hole electric current densities and carrier fluxes for two gates voltages along the same cut used previously, for our advanced model and when the electrochemical potentials are identical, i.e  $\gamma_n = \gamma_p = \gamma$ . This latter case (in dotted line) corresponds to the two-channel model. Clearly, electron and hole electric current densities and carrier fluxes cancel out at the edges of the Hall bar with our advanced model but they do not when  $\gamma_n = \gamma_p = \gamma$ , which is inconsistent for a finite Hall bar.

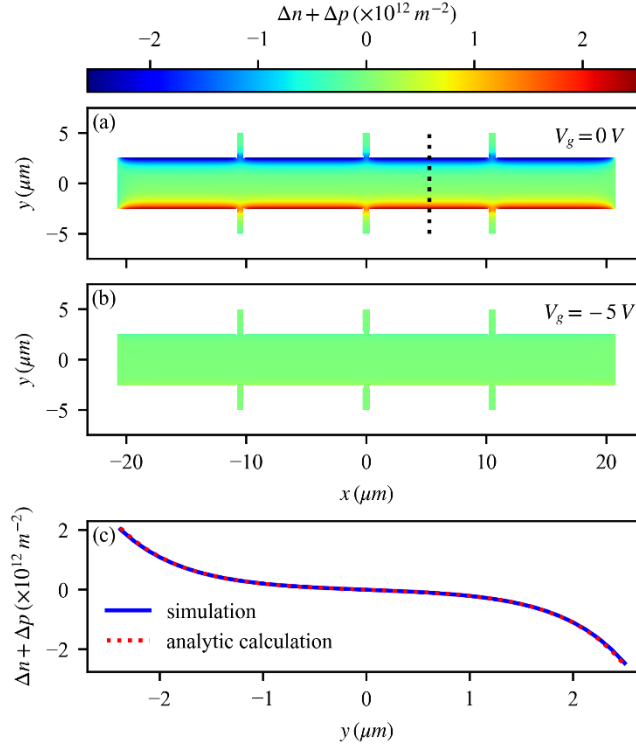


FIG. 4. (a) and (b), color map of  $\Delta n + \Delta p$  for two gate voltages. (c)  $\Delta n + \Delta p$  along the transverse cut (black dotted lines) represented on (a). The blue curve is the analytical expression (Eq. 11) and the red dotted lines is the simulated curve.

Figures 4(a)-4(b) show the variation of doping  $\Delta n + \Delta p = n - n_{eq} + p - p_{eq}$  for two gate voltages to focus on the occurrence of accumulation and depletion areas near the edges of the Hall bar. These areas are the sources of the transverse electron and hole diffusion fluxes  $P_{yD}$ . At low bias current and in the ambipolar regime ( $V_g = 0 \text{ V}$ ), these areas developed symmetrically with respect to the plane  $y = 0$  (Fig. 4(a)). At  $V_g = -5 \text{ V}$ , where hole doping is dominating, these areas are negligible. It can be demonstrated that the shape of  $\Delta n + \Delta p$  along the transverse direction fits very well at low bias current with the following expression (see Supplemental material [38] Sec. II) (blue curve in Fig. 4(c))

$$\Delta n + \Delta p = \mu^2 B \frac{\partial V_{gr}}{\partial x} \left( n_{eq} \frac{L_n}{D_n} \frac{sh\left(\frac{y}{L_n}\right)}{ch\left(\frac{W}{2L_n}\right)} + p_{eq} \frac{L_p}{D_p} \frac{sh\left(\frac{y}{L_p}\right)}{ch\left(\frac{W}{2L_p}\right)} \right) \quad (11)$$

With  $D_{n(p)}$  the diffusion coefficients of electrons (holes) which write

$$D_{n(p)} = \eta \frac{\pi \hbar^2 v_f^2 \mu}{e \int_{E_{CNP}}^{-\eta\infty} 2|E - E_{CNP}| \frac{\partial f}{\partial E} dE} n_{eq}(p_{eq}) \quad (12)$$

And  $L_{n(p)} = \sqrt{D_{n(p)} \tau_r}$  the diffusion lengths of the carriers (see Supplementary material [38] Sect. II). Equation 11 shows that the size of the accumulation and depletion areas are given by the diffusion length and their amplitude increases with magnetic field, bias current and carrier mobility.

## B. Bias current effect

In this part, we will focus on the effect of the bias current on the magnetic field sensitivity shape. We performed simulations on Hall bars having a  $\mu = 2 \text{ m}^2 / (\text{V} \cdot \text{s})$  and two different widths,  $W = 1 \mu\text{m}$  and  $W = 5 \mu\text{m}$ . We used  $W' = 2W$  and  $W_h = W/10$  to ease the comparison with the two-channel model which was established for an electrodeless Hall bar.

Figure 5 shows simulated  $S_I(V_g)$  and  $R_L(V_g)$  for 2 different bias current values,  $1 \mu\text{A}$  (black lines) and  $200 \mu\text{A}$  (red lines) and the two widths. First, we observe that the position of the CNP where  $R_L$  is maximum and  $S_I$  cancels out, shifts towards positive voltage values as the bias current increases. For the largest Hall bar, the maximum of  $R_L$  slightly decreases and the overall shape of  $S_I$  is not affected. For the smallest Hall bar, the maximum resistance strongly decreases and the shape of  $S_I$  is modified with the current. In particular, the amplitudes of the sensitivity extrema decrease and their gate voltage separation increases. These observations are very similar to our experimental ones (Fig. 1) and the experimental ones reported previously [6,11,17–19].

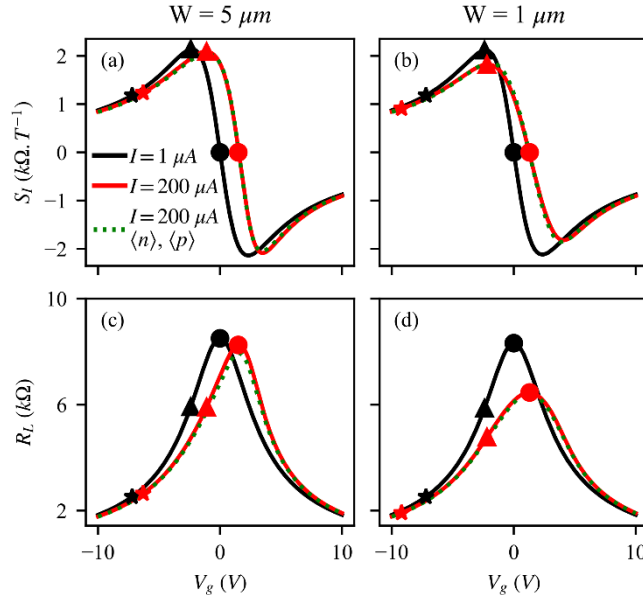


FIG. 5. (a), (b) Simulated  $S_I(V_g)$  for  $5 \mu\text{m}$  and  $1 \mu\text{m}$  width Hall bars at 2 different bias current values,  $1 \mu\text{A}$  (black curve) and  $200 \mu\text{A}$  (red curve). (c), (d) Corresponding simulated  $R_L(V_g)$ . The green dotted lines correspond to curves calculated using equation (1) for  $S_I$  and  $R = L/W e \mu (\langle n \rangle + \langle p \rangle)$  for  $R_L$  with  $\langle n \rangle$  and  $\langle p \rangle$  the simulated average values of  $n$  and  $p$  in the Hall bar.

To understand the CNP shift, in Fig. 6, the electrostatic potential  $V_{gr}$  as well as  $n$  and  $p$  are represented along the  $x$ -axis at  $y = 0 \mu\text{m}$ , for the two considered bias currents and three gate voltages corresponding to a strong positive doping (black and red star symbols), a doping where  $S_I$  is maximum (black and red triangular symbols) and a doping where  $S_I = 0$  (black and red circular symbols), i.e. at the CNP (only the  $5 \mu\text{m}$  width Hall bar is considered, but results are similar for the  $1 \mu\text{m}$  Hall bar, see Supplemental material [38] Sec. III, Fig. S3). We observe that  $V_{gr}$  decreases almost linearly along the bar whatever the bias current value. Regarding the doping, at low bias current, it is uniform in the channel and, as  $V_{gr}$  is of the order of few tenths of mV, it depends only on the gate voltage,  $Q_{gr} \approx -C_g V_g$  (see Eq. 4, Figs. 6(a)-6(c)). Hence the CNP gate voltage position corresponding to  $Q_{gr} = 0$  is  $V_{CNP} \approx 0 \text{ V}$  where  $n = p$  and are minimum in all the channel (Fig. 6(c)). At low bias current, our approach and the two-channel model are equivalent, confirming that the two-channel model is a good approximation in this case. Concerning high bias current,  $V_{gr}$  is of the order of magnitude of  $V_g$ . Hence the doping is no longer uniform (Fig. 6(d)-6(f)). For negative value of  $V_g$ , the electric charge and hence the doping increase near the drain electrode where the gate voltage adds with the drain voltage,  $Q_{gr} = -C_g(V_g - V_{gr})$  (see Eq. 4, Fig. 6(d) and 6(e)). For positive value of  $V_g$ , drain voltage and gate voltage have an opposite role, a  $p$ - $n$  junction appears in the channel (Fig. 6(f)) whose spatial position can be evaluated depending on  $V_g$  and  $V_{gr}$  using Eq. (4) with  $Q_{gr} = 0$ . Thus, for a given  $V_g$ , the  $x$  position of the  $p$ - $n$  junction is obtained when  $V_{gr}(x) = V_g$ . Therefore, observing that the CNP corresponds to the formation of the  $p$ - $n$  junction in the middle of the channel where  $V_{gr}(x) \approx V_D/2$  (Fig. 6(f)), we deduce that  $V_{CNP} \approx V_D/2 = R_{max}I/2$  with  $R_{max}$  the 2 probes maximum resistance. This conclusion is in agreement with previous experimental works [18]. It clearly confirms that the CNP gate voltage position is directly related to the bias current due to a doping modulation inside the device as reported for graphene field effect transistor [23,24].

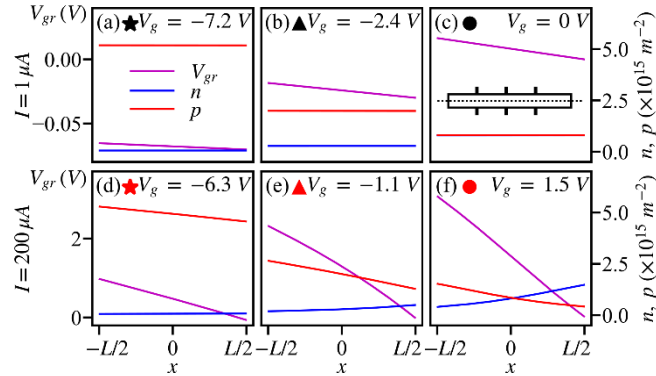


FIG. 6. Carrier doping  $n$  (blue curves) and  $p$  (red curves), electrostatic potential  $V_{gr}$  (violet curves) along  $x$  for  $y = 0 \mu\text{m}$  for the  $5 \mu\text{m}$  width Hall bar at three different gate voltage values (see star, triangular and circular symbols on Fig. 3) and for two bias current values,  $1 \mu\text{A}$  (a), (b), (c) and  $200 \mu\text{A}$  (d), (e), (f). Insert Fig. 6(c): location of the profiles on the Hall bar.

Regarding the bias current-induced evolution of the shape of  $S_I$  and  $R_L$  in particular for the smallest Hall bar (Fig. 5(b) and 5(d)), it will be demonstrated in the following that it is a direct consequence of the occurrence of the accumulation and depletion areas near the edges of the Hall bar as discussed in Sec. A. Their size is of the order of the charge carrier diffusion length  $L_{n(p)}$  which is identical for electrons and holes at the CNP and equals  $616 \text{ nm}$  with the parameters used for the simulation. To have an insight into this phenomenon, the Figs. 7(a)-7(h), show colour maps of  $n + p$  and  $\Delta n + \Delta p$  at gate voltages maximising  $S_I$  in the hole regime (black and red triangular symbols in Fig. 5), for both widths and both bias current values, while the Figs. 7(i)-(l) show profiles along the  $y$ -axis of  $n + p$  and  $\Delta n + \Delta p$  in the central part of the Hall bar (at  $x = 0 \mu\text{m}$ ). At low bias current and for both Hall bar widths, the hole accumulation and depletion areas are uniform all along the Hall bar and symmetric in amplitude with respect to the plane  $y = 0$  (Fig. 7(b) and 7(f)) which is consistent with the observation that the electric charge, which is principally controlled by the gate voltage at low bias current ( $Q_{gr} \approx -C_g V_g$ , see Eq. 4), must remain uniform. However, their amplitudes are negligible compared to the average value of the carrier doping (Figs. 7(a), 7(b), 7(i), 7(e), 7(f) and 7(k)) which is thus almost uniform inside the both Hall bars as we can observe on Figs. 7(a) and 7(e). On the Figs. 7(i) and 7(k), a focus is made on the central part of the Hall bar (at  $x = 0 \mu\text{m}$ ), we clearly observe that the average total carrier doping  $\langle n + p \rangle$  along  $y$  (marked by a black transverse dotted line on Figs. 7(a) and 7(e)) is equal in both Hall bars at low-bias current (red dotted lines Figs. 7(i) and 7(k)). It takes the value  $2.28 \times 10^{-15} \text{ m}^{-2}$

which is uniform in the Hall bar (Figs. 7(a) and 7(e)). At high bias current, the situation is more complex. For the largest Hall bar, we observe that the accumulation and depletion areas are almost symmetric in amplitude with respect to the plane  $y = 0$  but they are not uniform. Their amplitudes increase towards the source electrode (Fig. 7(d)) and are also more pronounced than at low bias current as expected (Figs. 7(c), 7(d) and 7(j)). However, the accumulation and depletion areas do not affect strongly the total carrier doping inside the Hall bar (Fig. 7(c)), whose non-uniformity is mainly induced by the amplitude of  $V_{gr}$  as explained in the previous paragraph ( $Q_{gr} = -C_g(V_g - V_{gr})$ , see Eq. 4). Figure 7(j) shows a focus on the central part (Fig. 7(c)). As explained for the low bias current case, the symmetry of the accumulation and depletion area amplitudes still leads to an average  $\langle n + p \rangle$  along  $y$  almost equals ( $2.32 \times 10^{-15} m^{-2}$ ) to the one at low-bias current (red dotted lines Fig. 7(i) and (j)). Therefore, since  $S_I$  is inversely proportional to  $n + p$  in the central part of the Hall bar, its amplitude barely varies at high bias current for the largest Hall bar (Fig. 5(a)). For the smallest Hall bar, Fig. 7(h) shows that the accumulation and depletion areas are non-symmetric in amplitude and non-uniform with a strongly dominant accumulation area on the bottom edge of the Hall bar whose amplitude is now of the order of magnitude of the total average carrier doping (Fig. 7(h)). Consequently, an important modification of the shape of  $n + p$  all along the Hall bar compared to the case at low bias current is observed (Figs. 7(e) and 7(g)). This phenomenon is related to the amplitude of  $L_{n(p)}$  which is of the order of magnitude of the Hall bar width leading to an important spreading of the accumulation and depletion areas inside the Hall bar. It results in a strong increase of the total carrier doping inside the Hall bar (Fig. 7(g)) and, as we observe in Fig. 7(l),  $\langle n + p \rangle$  averaged along  $y$  (red line Fig. 7(l)) increases strongly to  $2.8 \times 10^{-15} m^{-2}$ . Hence, a large decrease of  $S_I$  is observed (Fig. 5(b)). It is possible to quantitatively reproduce the shape of  $S_I$  as a function of gate voltage and bias current using the average simulated doping values  $\langle n \rangle$  and  $\langle p \rangle$  on the entire Hall bar and combined with Eq. 1 (green dotted lines on Fig. 5(a) and 5(b)). Thus, this analysis demonstrates the key role of the spatial profiles of the carrier doping  $n$  and  $p$  inside the Hall bar which depend on bias current, gate voltage, and Hall bar geometry.

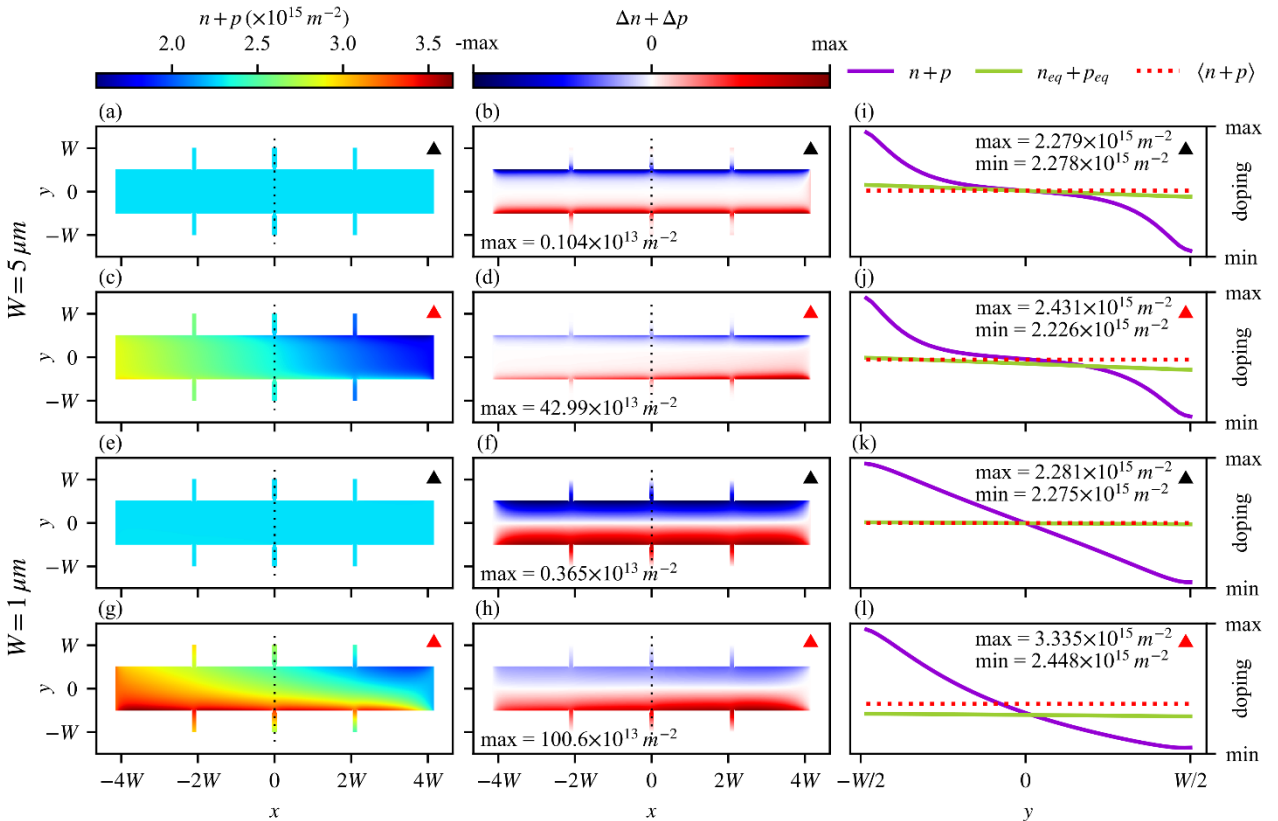


FIG. 7. Colour maps of  $n + p$  and  $\Delta n + \Delta p$  at the maximum amplitude of  $S_I$  in the hole regime for the large Hall bar at low bias current (a) and (b) and high bias current (c) and (d) and for the small Hall bar at low bias current (e) and (f) and high bias current (g) and (h). Transverse cut of  $n + p$  in the central part of the Hall bar (black dotted lines on figures (a)-(h)) for the large Hall bar at low bias current (i) and high bias current (j), and for the small Hall bar at low bias current (k) and high bias current (l).

Concerning  $R_L$ , a similar analysis can be done with maps of  $n + p$  at  $V_g = V_{CNP}$ . Figures 8b and 8f show that at low-bias current and for both Hall bar widths, the accumulation and depletion areas are perfectly symmetric with respect to the plane  $y = 0$ . As for  $S_I$ , it leads to a uniform and minimum average doping all along the two Hall bars equal to  $1.62 \times 10^{-15} m^{-2}$  (red dotted lines on Figs. 8(i) and 8(k)). For the largest Hall bar at high-bias current, as explained previously, we still observe symmetric accumulation and depletion areas (Fig. 8(d)) with a minimum doping in the centre of the Hall bar corresponding to the apparition of the  $p$ - $n$  junction (Fig. 8(c)).  $\langle n + p \rangle$  along  $y$  in the central part is equal to  $1.65 \times 10^{-15} m^{-2}$  (black dotted lines Fig. 8(c)), a value barely equal to the one at low-bias current (Figs. 8(i) and 8(j)). As a result, the resistance, which is inversely proportional to  $n + p$ , is nearly equal at low and high-bias current. For the smallest Hall bar, the shape of  $n + p$  is strongly affected by the bias current with a dominant accumulation area at the bottom edge of the Hall bar, resulting in an increase of the average value of  $n + p$  compared to the value at low-bias current (red lines on Figs. 8(k) and 8(l)) consistent with the maximum resistance decreases at high bias current (Fig. 5(d)). In the same way as for  $S_I$ , it is possible to quantitatively reproduce the shape of  $R_L$  as a function of gate voltage and bias current using the average simulated doping values  $\langle n \rangle$  and  $\langle p \rangle$  on the entire Hall bar and combined with the equation  $R = L/W e \mu (\langle n \rangle + \langle p \rangle)$  (green dotted lines in Fig. 5).

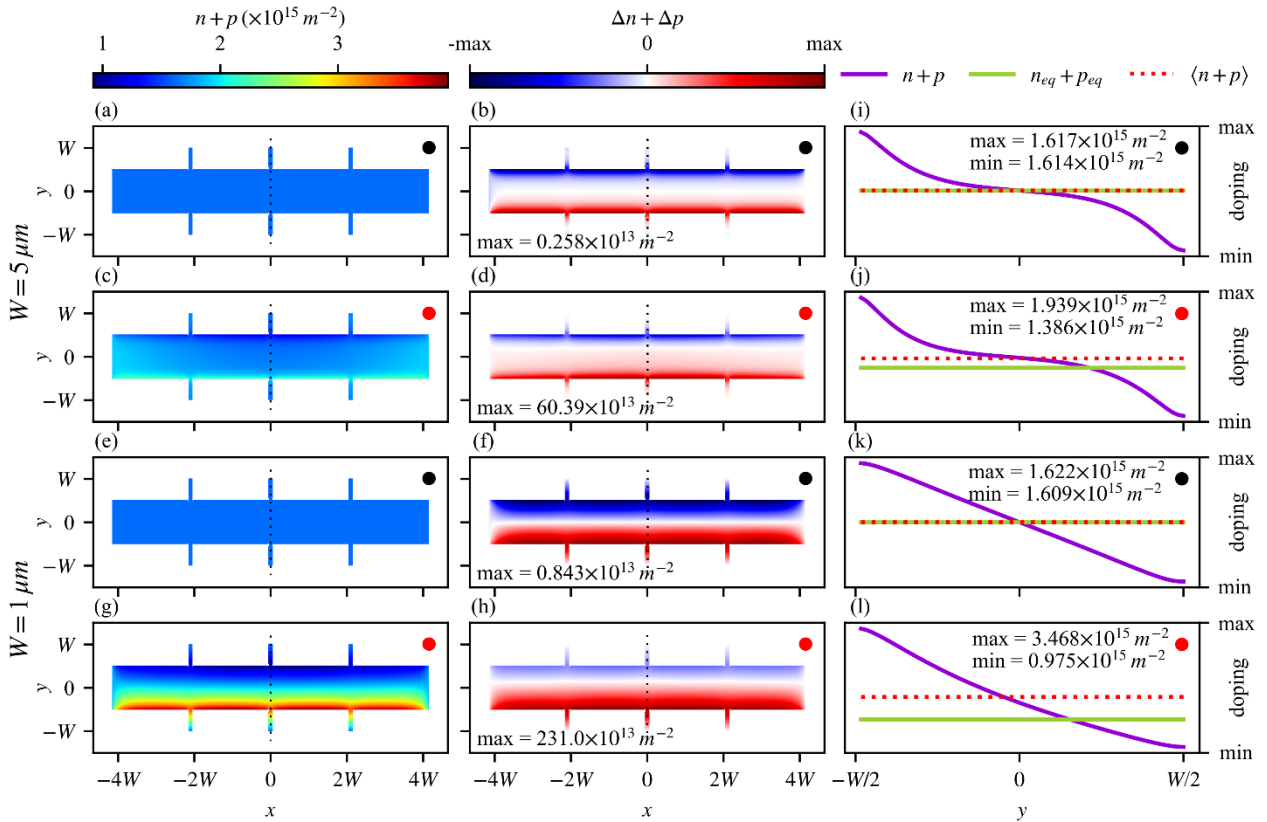


FIG. 8. Colour maps of  $n + p$  and  $\Delta n + \Delta p$  at the maximum amplitude of  $R_L$  for the large Hall bar at low bias current (a) and (b) and high bias current (c) and (d) and for the small Hall bar at low bias current (e) and (f) and high bias current (g) and (h). Transverse cut of  $n + p$  in the central part of the Hall bar (black dotted lines on figures (a)-(h)) for the large Hall bar at low bias current (i) and high bias current (j), and for the small Hall bar at low bias current (k) and high bias current (l).

To conclude this part, we performed simulations with an increased recombination-generation rate  $R'$  (using  $k' = 10k$ ) in order to clearly demonstrate that when the accumulation and depletion area amplitudes are decreased,  $S_I$  and  $R_L$  gate voltage and bias current dependences are less affected. We focused on the smallest GHS where the effect is more pronounced. Figure 9(a) shows that with  $k' = 10k$ , the shape of  $S_I$  is less affected at high bias current (blue curve), its maximum amplitude does not decrease strongly compared to the case at low bias current. Figure 9(b) shows the profile of  $n + p$  along a transverse cut at  $x = 0 \mu m$  for  $k$  and  $k'$ . It is clear that the accumulation and depletion areas are less pronounced when the recombination rate is high (for  $k'$ , blue curve) resulting in an average value of  $n + p$  closer to the equilibrium value. This observation is consistent with the decrease of  $L_{n(p)}$

which is equal for  $k'$  to 195 nm. Finally, this comparison of our model and the two-channel model clearly points out the shortcomings of the two-channel model and reveals the important role of the accumulation and depletion areas on the electrical characteristics of GHS.

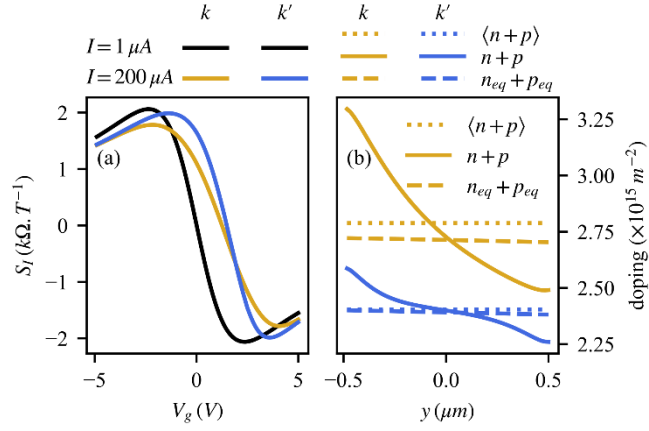


FIG. 9. (a) Magnetic field sensitivity  $S_I$  for two values of the bias current and two values of  $k$ . (b) Profile of  $n + p$  along a transverse cut at  $x = 0 \mu m$  at high bias current for two values of  $k$ .

### C. Electron-hole puddle effect

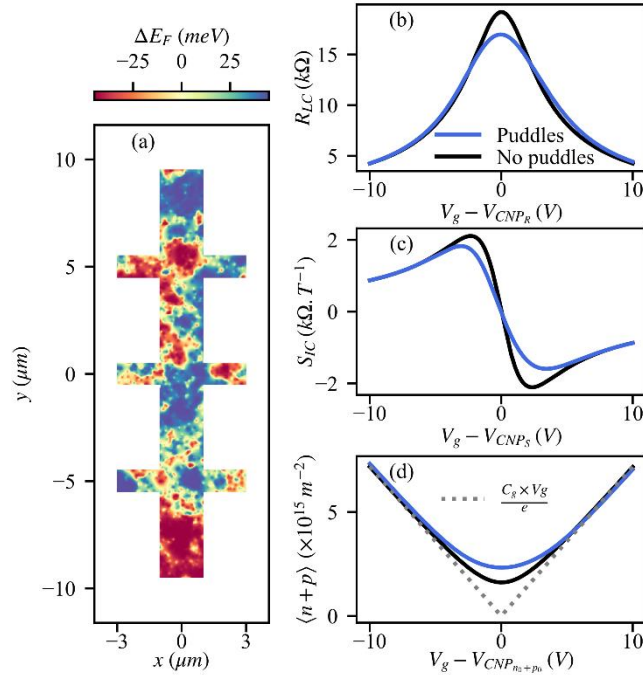


FIG. 10. (a) Colour map of the Fermi level fluctuations in the Hall bar induced by the random gate voltage fluctuations. The parameters used to generate the map were  $\Delta E_{fmax} = 45 meV$ ,  $20 nm < r_{0i} < 50 nm$  and  $n_{0l} = 3 \times 10^9 cm^{-2}$ . (b) and (c) Simulated longitudinal resistance  $R_{LC}$  and magnetic field sensitivity  $S_{IC}$  with puddles (blue curves) and without puddles (black curves). (d) Total average doping  $\langle n + p \rangle$  as a function of  $V_g$  with puddles (blue curves) and without puddles (black curves). The GHS being now strongly inhomogeneous, the positions of the CNP are slightly different for  $R_{LC}$ ,  $S_{IC}$  and  $\langle n + p \rangle$  and are noted  $V_{CNP_R}$ ,  $V_{CNP_S}$  and  $V_{CNP_{n_0+p_0}}$ .

Figure 10(a) shows a typical map of Fermi level fluctuations generated using Eq. (8) at  $V_g = 0 V$ . The used parameters are  $\Delta E_{frmax} = 45 meV$ ,  $r_{0i}$  ranging from 20 nm to 50 nm and  $n_{0l} = 3 \times 10^9 cm^{-2}$ . Fermi level fluctuations have a root mean square of 31 meV and induce a mean residual charge carrier doping  $\langle n + p \rangle$  of

$2.32 \times 10^{11} \text{ cm}^{-2}$ , a value above the thermal one equal to  $1.61 \times 10^{11} \text{ cm}^{-2}$ . The full width at half maximum (FWHM) of the autocorrelation map function allows to extract a mean puddle size of  $1 \mu\text{m}$ , meaning puddles span the Hall bar. Figures 10(b) and 10(c) show the compensated longitudinal resistance  $R_{LC}$  and magnetic field sensitivity  $S_{IC}$  simulated with and without puddles for  $W = 2 \mu\text{m}$ ,  $W' = 3W$ ,  $W_h = W/2$  and  $\mu = 1 \text{ m}^2/(\text{V}\cdot\text{s})$ . While the overall shape of  $R_{LC}$  and  $S_{IC}$  is preserved, the main effect of puddle introduction is to decrease both the resistance and sensitivity near the CNP as expected. For large gate voltages, corresponding to high doping and single carrier type behaviour (at  $|V_g| \gtrsim 5 \text{ V}$ ), there are no significant changes as the Fermi level fluctuations become negligible [26] (Fig. 10(d)). The chosen values of  $n_{0i}$  and  $r_{0i}$  were based on experimental observations of puddles [31,32,35] and the requirement that the Boltzmann formalism must remain valid. This implies that the conductivity should not vary on a length scale greater than the mean free path  $l_m$  [36] which mathematically means  $\sigma/\|\vec{\nabla}\sigma\| > 5l_m$  with  $l_m = \hbar\sqrt{\pi}\mu(n+p)/e(\sqrt{n} + \sqrt{p})$ . Under these conditions, 95% of the Hall bar surface satisfies the criterion.

## V. ANALYSIS OF THE EXPERIMENTAL RESULTS

For a proper comparison between experiments and simulations, the dimensions of the measured GHS were obtained with an atomic force microscope (see Supplemental material [38] Fig. S4).

### A. Analysis of the CVD GHS

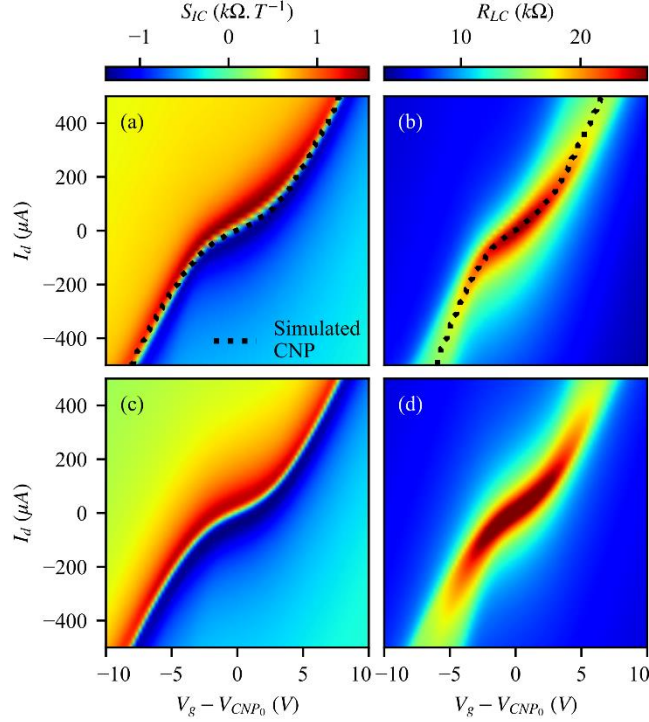


FIG. 11. Experimental maps of (a)  $R_{LC}$  and (b)  $S_{IC}$  for CVD-GHS ( $B = 1 \text{ T}$ ,  $T = 200 \text{ K}$ ), compared with simulations of (c)  $R_{LC}$  and (d)  $S_{IC}$  (see Table 1). The black dot lines in figures (a), (b) represent the simulated  $V_{CNP}$  extracted from (c), (d).  $V_{CNP0}$  is the CNP gate voltage position at the smallest bias current.

Figure 11 shows the experimental and simulated maps of  $R_{LC}$  and  $S_{IC}$  of the CVD-GHS as a function of bias current and gate voltage at  $T = 200 \text{ K}$  and  $B = 1 \text{ T}$ . Table 1 lists the parameters used for the simulation. For this device, in addition to long-range scatterers, short-range scatterers were introduced to reproduce the sublinear behaviour of the longitudinal conductance as a function of the gate voltage (see Supplemental material [38] Fig. S5(a)). Short-range scatterers induce resistivity  $\rho_{sr}$  independent of the electron and hole doping [39], hence the short range scatterer carrier mobility writes  $\mu_{sr}(E) = \pi(\hbar v_f)^2 / e\rho_{sr}|E - E_{CNP}|^2$ . The simulated data agree very well with the experimental ones: amplitudes of  $R_{LC}$  and  $S_{IC}$  are well reproduced together with their overall shapes, especially the CNP shift (see Supplemental material [38] Fig. S5). Indeed, the dotted lines on the Figs. 11(a) and

11(b) represent the  $V_{CNP}$  extracted from simulations. The mean residual charge carrier doping ( $n + p$ ) is about  $2.3 \times 10^{11} \text{ cm}^{-2}$ , a value much larger than the thermal one,  $7.4 \times 10^{10} \text{ cm}^{-2}$  which means that there is an important number of electron-hole puddles. This observation is coherent with the presence of impurities and defects observed on the Raman measurements (Fig. 1(a)) and the low mobility and large recombination-generation rate used for the simulations (Table 1). For this device, accumulation and depletion areas are negligible because of a diffusion length of 39 nm. The very good agreements between simulations and experiments show that our method of introducing electron-hole puddles is effective enough to analyse large samples with an important number of impurities.

TABLE 1. Parameters used for the comparison between experiments and simulations.

<i>Parameters</i>	<b>CVD</b>	<b>HOPG</b>	<b>hBN</b>
$t_{ox}(nm)$	105	280	300
$v_f(10^6 \text{ m/s})$	1	1.2	1.4
$\mu_{tr}(m^2/Vs)$	0.7	1.5	5
$\rho_{sr}(\Omega)$	1000	0	0
$n_{0l}(10^9 \text{ cm}^{-2})$	3	3	3
$r_{0i}(nm)$	50 - 80	60 - 100	60 - 100
$\Delta E_{fmax}(meV)$	85	18	15
$k(m^2/s)$	$10^{-2}$	$3.10^{-4}$	$1.10^{-5}$

## B. Analysis of the HOPG and hBN GHS

Figure 12 shows the experimental and simulated  $R_{LC}$  and  $S_{IC}$  of the HOPG and hBN-GHS for two bias current values,  $1 \mu A$  (black lines) and  $100 \mu A$  (red lines) for HOPG-GHS and  $2 \mu A$  (black lines) and  $200 \mu A$  (red lines) for hBN-GHS at  $T = 300 \text{ K}$  and  $B = 0.1 \text{ T}$ . With the exception of the  $R_{LC}$  amplitude of hBN-GHS at high current, the simulated data agree very well with the experimental ones. Importantly, the maxima of  $S_{IC}$  reaches  $3 \text{ k}\Omega/T$  and  $4 \text{ k}\Omega/T$  at low bias current for HOPG and hBN-GHS respectively. These values are larger than  $2 \text{ k}\Omega/T$ , the value expected at 300 K for a pristine graphene considering  $v_f = 10^6 \text{ m/s}$ , the most frequently used value of the Fermi velocity. This discrepancy means that the charge carrier density must be lower, i.e., the density of states must be lower and the Fermi velocity higher. Several studies of the electronic properties of graphene using angle-resolved photoemission spectroscopy (ARPES), STM or Terahertz measurements have shown that  $v_f$  can reach values as high as  $1.5 \times 10^6 \text{ m/s}$  [40–42]. Such renormalization of the Fermi velocity is mainly due to poorly screened electron-electron interactions in suspended graphene [43] and h-BN encapsulated graphene [40]. Accordingly, our simulations lead to  $v_f = 1.2 \times 10^6 \text{ m/s}$  and  $v_f = 1.4 \times 10^6 \text{ m/s}$  for HOPG and hBN-GHS respectively. These values are in agreements with previous works [40–42]. However, despite the total carrier density must be lower to explain the  $S_{IC}$  amplitude, it is still necessary to introduce electron-hole puddles to reproduce the measured  $R_{LC}$  and  $S_{IC}$  gate voltage dependences, especially at high-bias current. For HOPG-GHS, the combination of higher Fermi velocity and electron-hole puddles leads to a mean residual charge carrier doping ( $n + p$ ) of  $1.2 \times 10^{11} \text{ cm}^{-2}$ , a value slightly superior to  $1.1 \times 10^{11} \text{ cm}^{-2}$ , the value expected without puddles. For hBN-GHS, the mean residual charge carrier doping of  $8.3 \times 10^{10} \text{ cm}^{-2}$  remains almost unaffected although the presence of electron-hole puddles plays a role in the amplitude of the resistance at high bias current. Both values are lower than  $1.61 \times 10^{11} \text{ cm}^{-2}$ , the expected value for pristine graphene with  $v_f = 10^6 \text{ m/s}$ . It is worth noting that it was not necessary to introduce Fermi velocity renormalization for the CVD-GHS, because the number of carriers is larger, meaning the electron-electron interaction is screened efficiently. Concerning the shape of  $S_I$ , its large modulation at high current for both devices is well reproduced by our model. It means that accumulation and depletion areas play an important role for these devices, as described in the Sec. B. Indeed, unlike CVD-GHS, diffusion lengths at the CNP are  $345 \text{ nm}$  and  $4.32 \mu m$  for HOPG and hBN-GHS respectively, which is of the order or larger than the device width, as a direct consequence of larger mobility and smaller recombination rate for both samples compared to the CVD-GHS (Table 1). Thus, the good agreement between our advanced model and experiments highlights the importance to consider distinct Fermi levels and recombination-generation processes for electrons and holes in order to address the



evolution of  $S_{IC}$  at high-bias current. Additionally, a coherent evolution of the mean residual charge carrier, mobility, and recombination rate is observed for the three samples (Table 1). Indeed, as expected, the mobility increases as the mean residual charge carrier decreases [26,27] and the recombination rate decreases as the Fermi velocity and the quality of the device increase [29,30]. Moreover, the thermal carrier statistics used in our model allow us to emphasize the importance of considering the renormalization of the Fermi velocity to explain the amplitude of  $S_{IC}$ . Regarding the amplitude of  $R_{LC}$  that our model does not reproduce quantitatively for hBN-GHS, we believe that it may be related to the size of the electron-hole puddles, whose amplitude is similar to the width of the device, and to their shapes, particularly near the edges of the Hall bar, which our method cannot take into account and which have been shown to elongate at the edges [35]. This may also be linked to the use of linear recombination generation rates, whereas nonlinear processes are expected when the electron and hole populations are far from equilibrium near the edges of the Hall bar, particularly for GHS with high carrier mobility such as hBN-GHS.

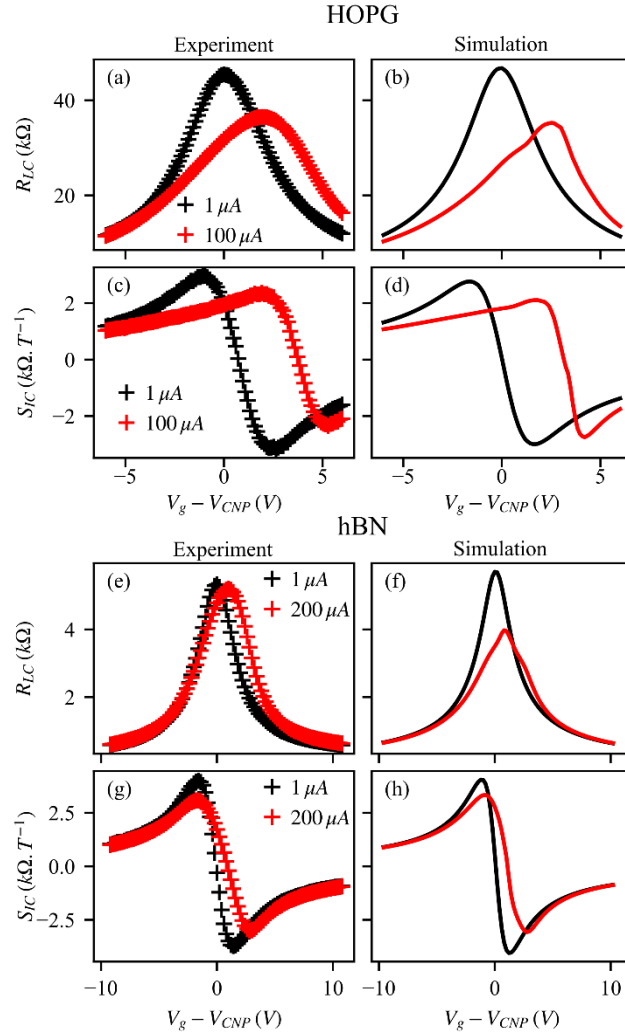


FIG. 12. Experimental (a) and (b) and simulated (e) and (f)  $R_{LC}$  and  $S_{IC}$  of the HOPG-GHS (black lines  $1 \mu A$ , red lines  $100 \mu A$ ). Experimental (c) and (d) and simulated (g) and (h)  $R_{LC}$  and  $S_{IC}$  of the hBN-GHS (black lines  $2 \mu A$ , red lines  $200 \mu A$ ). Both samples were measured at  $T = 300 K$  and  $B = 0.1 T$ .

## VI. CONCLUSION

In summary, we have developed a comprehensive numerical model with several improvements over the two-channel model: (i) our model considers the effect of temperature and different processes of charge carrier scattering, (ii) our model takes into account the spatial modulation of the carrier doping as a function of bias current, gate voltage, and geometry by using distinct Fermi levels for electrons and holes and a local field effect model for electrostatic doping, (iii) our model accounts for charge carrier inhomogeneities introduced by substrates and

contamination by using a semi-empirical method to locally introduce electron-hole puddles, unlike previous works where the influence of the puddles is treated on average [22,37]. Consequently, our advanced model can quantitatively reproduce the galvanomagnetic properties of GHS having different qualities and under different conditions of biasing, contrary to the two-channel model. In addition, an in-depth understanding of the operation principles and limitations of GHS is obtained. In particular, our model reveals how accumulation and depletion areas that form near the edges of the Hall bar in the ambipolar regime can affect and degrade the performance of GHS with widths of the order of the charge carrier diffusion length (see supplemental material [38], Fig. S6). It would therefore be interesting to compare the predicted performance of GHS a few hundred nanometers wide with their actual performance. Additionally, we demonstrate how the substrate and, more generally, the electrostatic environment of the graphene can affect the GHS performance through the variation of the Fermi velocity. This means that the use of substrates or encapsulation materials with low relative dielectric constants [42] or the use of suspended graphene [43] should improve performance. It is worth noting that Fermi velocity can also be modulated by in-plane uniform strain [44]. It could constitute another method to increase the magnetic field sensitivity of GHS. Despite the good agreements between the simulations and the experiments presented in the paper, further improvements can still be made. Indeed, our model has three input parameters, the value of the Fermi velocity, the expression of the recombination rate, and the map of the electron-hole puddles. First, regarding the value of the Fermi velocity, it will be very helpful to perform ARPES measurement on our samples to have a precise estimation and confirm its role. Second, the linear expression of the recombination-generation rate used in our model may be not relevant when the electron and hole populations are far from the equilibrium, especially for small high-quality samples biased with high bias current. Better agreements between simulations and experiments, particularly concerning the amplitude of the resistance, should be obtained for high quality samples if realistic and nonlinear processes are included, such as recombination-generation induced by optical phonons [30]. Future work will be carried out in this sense. Regarding the map of the electron-hole puddles, it should be helpful to integrate real maps measured under various conditions and different substrates using near-field photocurrent nanoscopy for example [35], especially to have a proper modelling of the electron-hole puddle size and shape inside the Hall bar [35]. This last point would allow us to obtain better agreements between simulations and experiments, particularly for small high-quality samples where the exact map of electron-holes puddles, whose sizes are of the order of magnitude of the width of the Hall bar, can have a strong influence on the shape of  $R_{LC}$  and  $S_{IC}$ . Finally, it is worth to note that recently, a Hall sensor made with an heterostructure of h-BN/MoS<sub>2</sub> was realised [45], our advanced model could be very helpful to study in detail the operation of such sensor as it is straightforward to adapt it to take into account a different electronic band structure, carrier mobility energy dependence and recombination-generation rate.

## ACKNOWLEDGMENTS

The authors thank Ioannis Paradisanos, Mathieu Pierre, and Walter Escoffier for fruitful discussions. This study has been supported through the EUR grant NanoX n° ANR-17-EURE-0009 in the framework of the “Programme des Investissements d’Avenir”.

## References

- [1] L. Theil Kuhn, A. K. Geim, J. G. S. Lok, P. Hedegård, K. Ylänen, J. B. Jensen, E. Johnson, and P. E. Lindelof, *Magnetisation of Isolated Single Crystalline Fe-Nanoparticles Measured by a Ballistic Hall Micro-Magnetometer*, Eur. Phys. J. D **10**, 259 (2000).
- [2] A. K. Geim, S. V. Dubonos, J. G. S. Lok, I. V. Grigorieva, J. C. Maan, L. T. Hansen, and P. E. Lindelof, *Ballistic Hall Micromagnetometry*, Appl. Phys. Lett. **71**, 2379 (1997).
- [3] R. S. Popović, *Hall Effect Devices*, 2. ed (Institute of Physics Publ, Bristol, 2004).
- [4] B. Chen, L. Huang, X. Ma, L. Dong, Z. Zhang, and L.-M. Peng, *Exploration of Sensitivity Limit for Graphene Magnetic Sensors*, Carbon **94**, 585 (2015).
- [5] D. Collomb, P. Li, and S. Bending, *Frontiers of Graphene-Based Hall-Effect Sensors*, J. Phys.: Condens. Matter **33**, 243002 (2021).
- [6] B. T. Schaefer, L. Wang, A. Jarjour, K. Watanabe, T. Taniguchi, P. L. McEuen, and K. C. Nowack, *Magnetic Field Detection Limits for Ultraclean Graphene Hall Sensors*, Nat Commun **11**, 4163 (2020).
- [7] K. S. Novoselov, *Electric Field Effect in Atomically Thin Carbon Films*, Science **306**, 666 (2004).
- [8] L. Wang et al., *One-Dimensional Electrical Contact to a Two-Dimensional Material*, Science **342**, 614 (2013).
- [9] V. Panchal, K. Cedergren, R. Yakimova, A. Tzalenchuk, S. Kubatkin, and O. Kazakova, *Small Epitaxial Graphene Devices for Magnetosensing Applications*, J. Appl. Phys. **111**, 07E509 (2012).

- [10] J. Dauber, A. A. Sagade, M. Oellers, K. Watanabe, T. Taniguchi, D. Neumaier, and C. Stampfer, *Ultra-Sensitive Hall Sensors Based on Graphene Encapsulated in Hexagonal Boron Nitride*, Appl. Phys. Lett. **106**, 193501 (2015).
- [11] M.-K. Joo, J. Kim, J.-H. Park, V. L. Nguyen, K. K. Kim, Y. H. Lee, and D. Suh, *Large-Scale Graphene on Hexagonal-BN Hall Elements: Prediction of Sensor Performance without Magnetic Field*, ACS Nano **9** (2016).
- [12] D. Collomb, P. Li, and S. J. Bending, *Nanoscale Graphene Hall Sensors for High-Resolution Ambient Magnetic Imaging*, Sci Rep **9**, 14424 (2019).
- [13] P. Li, D. Collomb, Z. J. Lim, S. Dale, P. Shepley, G. Burnell, and S. J. Bending, *High Resolution Magnetic Microscopy Based on Semi-Encapsulated Graphene Hall Sensors*, Appl. Phys. Lett. **121**, 043502 (2022).
- [14] M. Kim et al., *Hall Micromagnetometry of Individual Two-Dimensional Ferromagnets*, Nat Electron **2**, 457 (2019).
- [15] V. Panchal, D. Cox, R. Yakimova, and O. Kazakova, *Epitaxial Graphene Sensors for Detection of Small Magnetic Moments*, IEEE Transactions on Magnetics **49**, 97 (2013).
- [16] G. Song, M. Ranjbar, and R. A. Kiehl, *Operation of Graphene Magnetic Field Sensors near the Charge Neutrality Point*, Commun Phys **2**, 65 (2019).
- [17] J. Kim and J. Na, *Low-Voltage-Operated Highly Sensitive Graphene Hall Elements by Ionic Gating*, 7 (2019).
- [18] L. Huang, Z. Zhang, B. Chen, X. Ma, H. Zhong, and L.-M. Peng, *Ultra-Sensitive Graphene Hall Elements*, Appl. Phys. Lett. **104**, 183106 (2014).
- [19] Dankert André, *Hall Sensors Batch-Fabricated on All-CVD h-BN/Graphene/h-BN Heterostructures*, Scientific Reports **7** (2017).
- [20] D. G. Purdie, N. M. Pugno, T. Taniguchi, K. Watanabe, A. C. Ferrari, and A. Lombardo, *Cleaning Interfaces in Layered Materials Heterostructures*, Nat Commun **9**, 5387 (2018).
- [21] *Graphene Number of Layers Calculator From ID/IG and I2D/IG Ratio via Raman Spectroscopy - InstaNANO*, <https://instanano.com/all/characterization/raman/graphene-layers/>.
- [22] I. Meric, M. Y. Han, A. F. Young, B. Ozyilmaz, P. Kim, and K. L. Shepard, *Current Saturation in Zero-Bandgap, Top-Gated Graphene Field-Effect Transistors*, Nature Nanotech **3**, 654 (2008).
- [23] J. G. Champlain, *A First Principles Theoretical Examination of Graphene-Based Field Effect Transistors*, J. Appl. Phys. **109**, 084515 (2011).
- [24] S. A. Thiele, J. A. Schaefer, and F. Schwierz, *Modeling of Graphene Metal-Oxide-Semiconductor Field-Effect Transistors with Gapless Large-Area Graphene Channels*, J. Appl. Phys. **107**, 094505 (2010).
- [25] F. A. Chaves, D. Jiménez, A. A. Sagade, W. Kim, J. Riikonen, H. Lipsanen, and D. Neumaier, *A Physics-Based Model of Gate-Tunable Metal-Graphene Contact Resistance Benchmarked against Experimental Data*, 2D Mater. **2**, 025006 (2015).
- [26] S. Adam, E. H. Hwang, V. M. Galitski, and S. Das Sarma, *A Self-Consistent Theory for Graphene Transport*, Proceedings of the National Academy of Sciences **104**, 18392 (2007).
- [27] T. Stauber, N. M. R. Peres, and F. Guinea, *Electronic Transport in Graphene: A Semi-Classical Approach Including Midgap States*, Phys. Rev. B **76**, 205423 (2007).
- [28] P. S. Alekseev, A. P. Dmitriev, I. V. Gornyi, V. Yu. Kachorovskii, B. N. Narozhny, M. Schütt, and M. Titov, *Magnetoresistance in Two-Component Systems*, Phys. Rev. Lett. **114**, 156601 (2015).
- [29] F. Rana, *Electron-Hole Generation and Recombination Rates for Coulomb Scattering in Graphene*, Phys. Rev. B **76**, 155431 (2007).
- [30] F. Rana, P. A. George, J. H. Strait, J. Dawlaty, S. Shivaraman, M. Chandrashekhara, and M. G. Spencer, *Carrier Recombination and Generation Rates for Intravalley and Intervalley Phonon Scattering in Graphene*, Phys. Rev. B **79**, 115447 (2009).
- [31] J. Martin, N. Akerman, G. Ulbricht, T. Lohmann, J. H. Smet, K. von Klitzing, and A. Yacoby, *Observation of Electron-Hole Puddles in Graphene Using a Scanning Single-Electron Transistor*, Nature Phys **4**, 144 (2008).
- [32] S. Samaddar, I. Yudhistira, S. Adam, H. Courtois, and C. B. Winkelmann, *Charge Puddles in Graphene near the Dirac Point*, Phys. Rev. Lett. **116**, 126804 (2016).
- [33] F. Guinea, M. I. Katsnelson, and M. A. H. Vozmediano, *Midgap States and Charge Inhomogeneities in Corrugated Graphene*, Phys. Rev. B **77**, 075422 (2008).
- [34] Y.-W. Tan, Y. Zhang, K. Bolotin, Y. Zhao, S. Adam, E. H. Hwang, S. Das Sarma, H. L. Stormer, and P. Kim, *Measurement of Scattering Rate and Minimum Conductivity in Graphene*, Phys. Rev. Lett. **99**, 246803 (2007).
- [35] A. Woessner et al., *Near-Field Photocurrent Nanoscopy on Bare and Encapsulated Graphene*, Nat Commun **7**, 10783 (2016).
- [36] E. Rossi, S. Adam, and S. Das Sarma, *Effective Medium Theory for Disordered Two-Dimensional Graphene*, Phys. Rev. B **79**, 245423 (2009).
- [37] J. Ping, I. Yudhistira, N. Ramakrishnan, S. Cho, S. Adam, and M. S. Fuhrer, *Disorder-Induced Magnetoresistance in a Two-Dimensional Electron System*, Phys. Rev. Lett. **113**, 047206 (2014).
- [38] See Supplemental Material at <http://link.aps.org/supplemental/>... for the random gate voltage fluctuations; the comparison with the two-channel model; the longitudinal profile of  $V_{gr}$ ,  $n$  and  $p$  for the 1  $\mu\text{m}$  wide Hall bar; the AFM images of the GHS; the CVD electrical characteristics; the performance degradation with width decrease.

- [39] N. H. Shon and T. Ando, *Quantum Transport in Two-Dimensional Graphite System*, J. Phys. Soc. Jpn. **67**, 2421 (1998).
- [40] C. Hwang, D. A. Siegel, S.-K. Mo, W. Regan, A. Ismach, Y. Zhang, A. Zettl, and A. Lanzara, *Fermi Velocity Engineering in Graphene by Substrate Modification*, Sci Rep **2**, 590 (2012).
- [41] J. Chae et al., *Renormalization of the Graphene Dispersion Velocity Determined from Scanning Tunneling Spectroscopy*, Phys. Rev. Lett. **109**, 116802 (2012).
- [42] P. R. Whelan et al., *Fermi Velocity Renormalization in Graphene Probed by Terahertz Time-Domain Spectroscopy*, 2D Mater. **7**, 035009 (2020).
- [43] D. C. Elias et al., *Dirac Cones Reshaped by Interaction Effects in Suspended Graphene*, Nature Phys **7**, 701 (2011).
- [44] M. Oliva-Leyva and G. G. Naumis, *Generalizing the Fermi Velocity of Strained Graphene from Uniform to Nonuniform Strain*, Physics Letters A **379**, 2645 (2015).
- [45] M.-K. Joo, J. Kim, G. Lee, H. Kim, Y. H. Lee, and D. Suh, *Feasibility of Ultra-Sensitive 2D Layered Hall Elements*, 2D Mater. **4**, 021029 (2017).

# Supplemental material

## Performance of graphene Hall effect sensors: role of bias current, disorder and Fermi velocity

Lionel Petit<sup>1</sup>, Tom Fournier<sup>1,2</sup>, Géraldine Ballon<sup>1</sup>, Cédric Robert<sup>1</sup>, Delphine Lagarde<sup>1</sup>, Pascal Puech<sup>2</sup>, Thomas Blon<sup>1</sup> and Benjamin Lassagne<sup>1</sup>

<sup>1</sup> Université de Toulouse, INSA-CNRS-UPS, LPCNO, 135 Av. Ranguéil, 31077 Toulouse, France

<sup>2</sup> Centre d'Elaboration des Matériaux et d'Etudes Structurales (CEMES), UPR8011 CNRS, Université Toulouse 3, 31055 Toulouse, France

E-mail: [lassagne@insa-toulouse.fr](mailto:lassagne@insa-toulouse.fr)

### I) Random gate voltage fluctuations

To convert the Fermi level fluctuations into gate voltage fluctuations we used Eq. 4 at zero gate voltage and zero bias current. Hence, the electrochemical potentials of electrons and holes are null,  $\gamma_n = \gamma_p = 0$  and as  $W_M = W_{gr}$ ,  $\Delta E_{fr} = eV_{gr}$ . Using  $Q_0 = 0$ , we can write

$$\Delta V_g = \frac{\Delta E_{fr}}{e} + \frac{e}{C_g} (n(\Delta E_{fr}) - p(\Delta E_{fr})) \quad (s1)$$

### II) Comparison with the two-channel model

At low magnetic field, low bias current and for a constant  $\mu$ , the conductivity components write

$$\sigma_{xxn(p)} \approx \frac{\eta e \mu}{\pi v_f^2 \hbar^2} \int_{E_{CNP}}^{-\eta \times \infty} (E - E_{CNP})^2 \frac{\partial f_{n(p)}}{\partial E} dE = en(p)\mu$$
$$\sigma_{xy_{n(p)}} \approx \frac{e \mu^2 B}{\pi v_f^2 \hbar^2} \int_{E_{CNP}}^{-\eta \times \infty} (E - E_{CNP})^2 \frac{\partial f_{n(p)}}{\partial E} dE = \eta en(p)\mu^2 B$$

The electric current densities and the carrier flux write in the two-channel model as follow

$$\vec{J}_n = -e\vec{P}_n = -en\mu \begin{vmatrix} \frac{\partial V_{gr}}{\partial x} - \mu B \frac{\partial V_{gr}}{\partial y} \\ \mu B \frac{\partial V_{gr}}{\partial x} + \frac{\partial V_{gr}}{\partial y} \end{vmatrix} \quad (s2a)$$

$$\vec{J}_p = e\vec{P}_p = -ep\mu \begin{vmatrix} \frac{\partial V_{gr}}{\partial x} + \mu B \frac{\partial V_{gr}}{\partial y} \\ -\mu B \frac{\partial V_{gr}}{\partial x} + \frac{\partial V_{gr}}{\partial y} \end{vmatrix} \quad (s2b)$$

Hence the total electric current density and the total carrier flux write

$$\vec{J} = \begin{vmatrix} -en\mu(n+p) \frac{\partial V_{gr}}{\partial x} + e(n-p)\mu^2 B \frac{\partial V_{gr}}{\partial y} \\ -e(n-p)\mu^2 B \frac{\partial V_{gr}}{\partial x} - e(n+p)\mu \frac{\partial V_{gr}}{\partial y} \end{vmatrix} \quad (s3a)$$

$$\vec{P} = \begin{vmatrix} (n-p)\mu \frac{\partial V_{gr}}{\partial x} - (n+p)\mu^2 B \frac{\partial V_{gr}}{\partial y} \\ (n+p)\mu^2 B \frac{\partial V_{gr}}{\partial x} + (n-p)\mu \frac{\partial V_{gr}}{\partial y} \end{vmatrix} \quad (s3b)$$

In our advanced model, the electric current densities and carrier flux write

$$\vec{J}_n = -e\vec{P}_n = n\mu \begin{vmatrix} \frac{\partial \gamma_n}{\partial x} - \mu B \frac{\partial \gamma_n}{\partial y} \\ \mu B \frac{\partial \gamma_n}{\partial x} + \frac{\partial \gamma_n}{\partial y} \end{vmatrix} \quad (s4a)$$

$$\vec{J}_p = e\vec{P}_p = p\mu \begin{vmatrix} \frac{\partial \gamma_p}{\partial x} + \mu B \frac{\partial \gamma_p}{\partial y} \\ -\mu B \frac{\partial \gamma_p}{\partial x} + \frac{\partial \gamma_p}{\partial y} \end{vmatrix} \quad (s4b)$$

Hence, the total electric current density and carrier flux expressions are

$$\vec{J} = \begin{vmatrix} \mu \left( n \frac{\partial E_{fn}}{\partial x} + p \frac{\partial E_{fp}}{\partial x} \right) - e(n+p)\mu \frac{\partial V_{gr}}{\partial x} - \mu^2 B \left( n \frac{\partial E_{fn}}{\partial y} - p \frac{\partial E_{fp}}{\partial y} \right) + e(n-p)\mu^2 B \frac{\partial V_{gr}}{\partial y} \\ \mu^2 B \left( n \frac{\partial E_{fn}}{\partial x} - p \frac{\partial E_{fp}}{\partial x} \right) - e(n-p)\mu^2 B \frac{\partial V_{gr}}{\partial x} + \mu \left( n \frac{\partial E_{fn}}{\partial y} + p \frac{\partial E_{fp}}{\partial y} \right) - e(n+p)\mu \frac{\partial V_{gr}}{\partial y} \end{vmatrix} \quad (s5a)$$

$$\vec{P} = \begin{vmatrix} -\frac{\mu}{e} \left( n \frac{\partial E_{fn}}{\partial x} - p \frac{\partial E_{fp}}{\partial x} \right) + (n-p)\mu \frac{\partial V_{gr}}{\partial x} + \frac{\mu^2 B}{e} \left( n \frac{\partial E_{fn}}{\partial y} + p \frac{\partial E_{fp}}{\partial y} \right) - (n+p)\mu^2 B \frac{\partial V_{gr}}{\partial y} \\ -\frac{\mu^2 B}{e} \left( n \frac{\partial E_{fn}}{\partial x} + p \frac{\partial E_{fp}}{\partial x} \right) + (n+p)\mu^2 B \frac{\partial V_{gr}}{\partial x} - \frac{\mu}{e} \left( n \frac{\partial E_{fn}}{\partial y} - p \frac{\partial E_{fp}}{\partial y} \right) + (n-p)\mu \frac{\partial V_{gr}}{\partial y} \end{vmatrix} \quad (s5b)$$

At low bias current, all the first terms of Eqs. s5(a) and s5(b) depending on the gradient of the Fermi levels along  $x$  ( $\frac{\partial E_{fn}}{\partial x}, \frac{\partial E_{fp}}{\partial x}$ ) can be neglected as they are almost null.

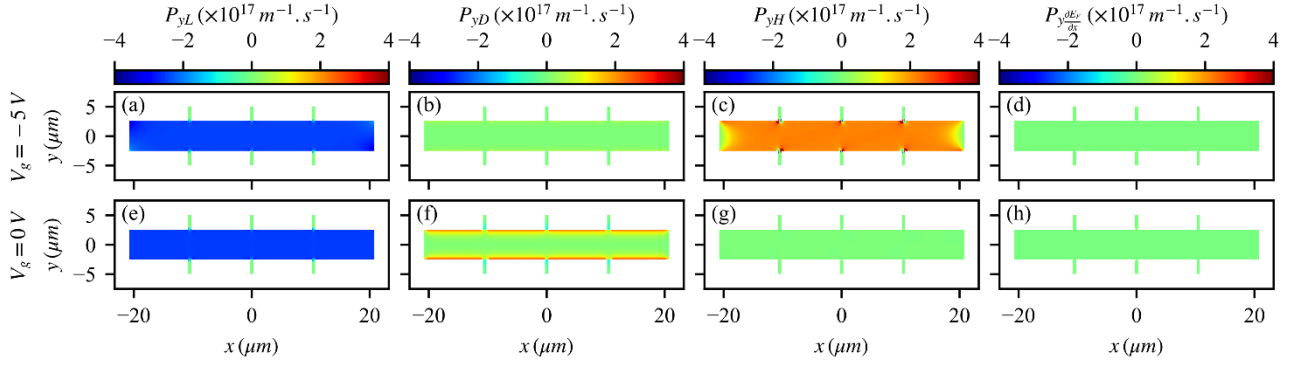


FIG. S1. (a) and (e), Lorentz component of the transverse carrier flux, (b) and (f), Diffusion component, (c) and (g) Hall component, (d) and (h) components depending on  $\frac{\partial E_{fn}}{\partial x}$  and  $\frac{\partial E_{fp}}{\partial x}$  for two gate voltages.

In the following, we consider the device operating at the CNP and supplied with a low bias current, typically few  $\mu\text{A}$ . The electron and hole doping spatial variations are expressed as follows

$$n = n_{eq} + \Delta n$$

$$p = p_{eq} + \Delta p$$

$n_{eq}$  and  $p_{eq}$  are the electron and hole doping at equilibrium. At low bias current, the doping variations are small, meaning that  $\Delta n \ll n_{eq}$  and  $\Delta p \ll p_{eq}$ . The spatial dependences of the carrier flux  $\vec{P}_n$  and  $\vec{P}_p$  are governed by the following relationships

$$-\vec{\nabla} \cdot \vec{P}_{n(p)} - R = 0 \quad (\text{s6})$$

With  $R = k(np - n_{eq}p_{eq})$ . At the CNP we assume that  $\Delta n = \Delta p$ , therefore we can write

$$R \approx k(\Delta n p_{eq} + \Delta p n_{eq}) = \frac{\Delta n}{\tau_r} = \frac{\Delta p}{\tau_r} \quad (\text{s7})$$

With  $\tau_r = 1/k(p_{eq} + n_{eq})$  the recombination rate. Injecting the relationships  $\vec{P}_{n(p)} = \frac{\eta}{e} \vec{J}_{n(p)}$  and Eq. s7 into Eq. s6, and assuming that  $\frac{\partial^2 \gamma_{n(p)}}{\partial x \partial y} = \frac{\partial^2 \gamma_{n(p)}}{\partial y \partial x}$  we can obtain the following relationships

$$\frac{n_{eq} \mu}{e} \left( \frac{\partial^2 \gamma_n}{\partial x^2} + \frac{\partial^2 \gamma_n}{\partial y^2} \right) - \frac{\Delta n}{\tau_r} = 0 \quad (\text{s8a})$$

$$-\frac{p_{eq} \mu}{e} \left( \frac{\partial^2 \gamma_p}{\partial x^2} + \frac{\partial^2 \gamma_p}{\partial y^2} \right) - \frac{\Delta p}{\tau_r} = 0 \quad (\text{s8b})$$

The simulations performed at the CNP ( $V_g = 0\text{V}$ ) reveal that in almost the entire Hall bar (Fig. S2):

$$\frac{\partial E_{fn}}{\partial x}, \frac{\partial E_{fp}}{\partial x}, \frac{\partial V_{gr}}{\partial y}, \frac{\partial^2 V_{gr}}{\partial x^2} \approx 0$$

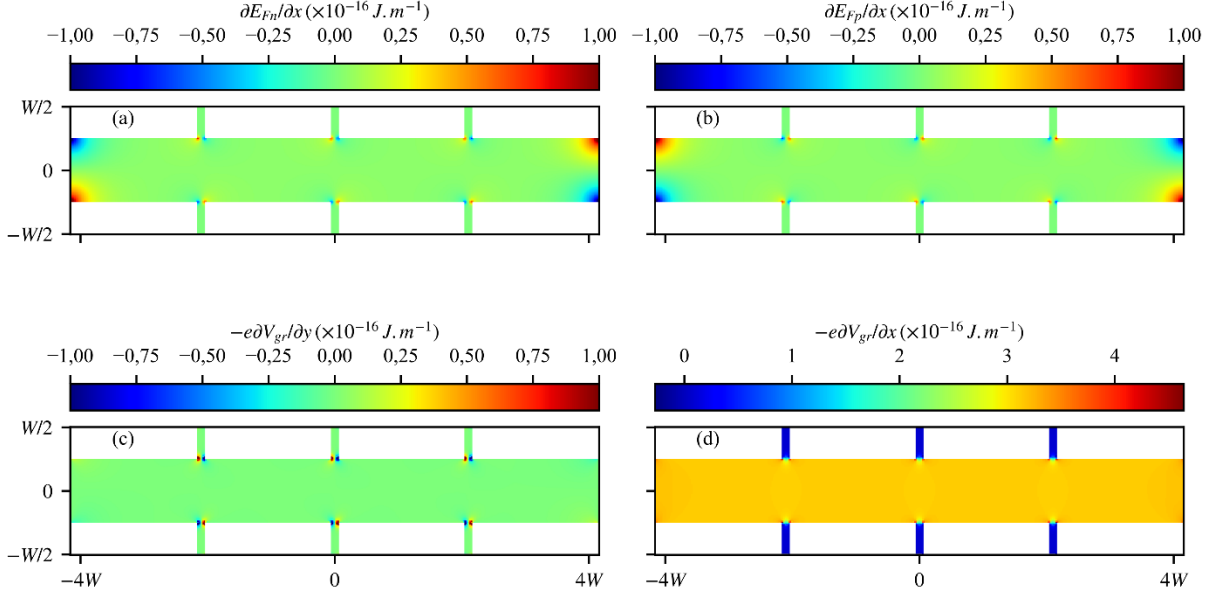


FIG. S2. Color maps of  $\frac{\partial E_{fn}}{\partial x}$  (a),  $\frac{\partial E_{fp}}{\partial x}$  (b)  $\frac{\partial V_{gr}}{\partial y}$  (c) and  $\frac{\partial V_{gr}}{\partial x}$  (d).

Hence the Eqs. s8(a) and s8(b) become

$$\frac{n_{eq}\mu}{e} \frac{\partial^2 E_{fn}}{\partial y^2} - \frac{\Delta n}{\tau_r} = 0 \quad (s9a)$$

$$-\frac{p_{eq}\mu}{e} \frac{\partial^2 E_{fp}}{\partial y^2} - \frac{\Delta p}{\tau_r} = 0 \quad (s9b)$$

We remind that

$$n = \int_{E_{CNP}}^{\infty} f(E - E_{fn}) \frac{2|E - E_{CNP}|}{\pi(\hbar v_f)^2} dE$$

$$p = \int_{-\infty}^{E_{CNP}} (1 - f(E - E_{fp})) \frac{2|E - E_{CNP}|}{\pi(\hbar v_f)^2} dE$$

Hence, the first derivatives of  $n$  and  $p$  write

$$\frac{\partial n}{\partial y} = -\frac{\partial E_{fn}}{\partial y} \int_{E_{CNP}}^{\infty} \frac{2|E - E_{CNP}|}{\pi(\hbar v_f)^2} \frac{\partial f}{\partial E} dE \quad (s10a)$$

$$\frac{\partial p}{\partial y} = \frac{\partial E_{fp}}{\partial y} \int_{-\infty}^{E_{CNP}} \frac{2|E - E_{CNP}|}{\pi(\hbar v_f)^2} \frac{\partial f}{\partial E} dE \quad (s10b)$$



And the second derivatives write

$$\frac{\partial^2 n}{\partial y^2} = -\frac{\partial^2 E_{fn}}{\partial y^2} \int_{E_{CNP}}^{\infty} \frac{2|E - E_{CNP}|}{\pi(\hbar v_f)^2} \frac{\partial f}{\partial E} dE + \left(\frac{\partial E_{fn}}{\partial y}\right)^2 \int_{E_{CNP}}^{\infty} \frac{2|E - E_{CNP}|}{\pi(\hbar v_f)^2} \frac{\partial^2 f}{\partial E^2} dE \quad (s11a)$$

$$\frac{\partial^2 p}{\partial y^2} = \frac{\partial^2 E_{fp}}{\partial y^2} \int_{-\infty}^{E_{CNP}} \frac{2|E - E_{CNP}|}{\pi(\hbar v_f)^2} \frac{\partial f}{\partial E} dE - \left(\frac{\partial E_{fp}}{\partial y}\right)^2 \int_{-\infty}^{E_{CNP}} \frac{2|E - E_{CNP}|}{\pi(\hbar v_f)^2} \frac{\partial^2 f}{\partial E^2} dE \quad (s11b)$$

The second terms of the Eqs. s11(a) and s11(b) are negligible, then we can convert the Eqs. s9(a) and s9(b) as follow

$$D_n \frac{\partial^2 n}{\partial y^2} - \frac{\Delta n}{\tau_r} = 0 \quad (s12b)$$

$$D_p \frac{\partial^2 p}{\partial y^2} - \frac{\Delta p}{\tau_r} = 0 \quad (s12b)$$

Where  $D_n$  and  $D_p$  are the diffusion coefficient of electrons and holes which write

$$D_n = \frac{\pi(\hbar v_f)^2 n_{eq} \mu}{e \int_{E_{CNP}}^{\infty} 2|E - E_{CNP}| \left(-\frac{\partial f}{\partial E}\right) dE} \quad (s13a)$$

$$D_p = \frac{\pi(\hbar v_f)^2 p_{eq} \mu}{e \int_{-\infty}^{E_{CNP}} 2|E - E_{CNP}| \left(-\frac{\partial f}{\partial E}\right) dE} \quad (s13b)$$

We can verify that at  $T = 0$  K,  $D_{n(p)} = \hbar v_f \sqrt{\pi n_{eq}(p_{eq})} \mu / 2e$ . The solutions of Eqs. s12(a) and s12(b) take the following forms

$$\Delta n = A e^{\frac{y}{L_n}} + A' e^{-\frac{y}{L_n}} \quad (s14a)$$

$$\Delta p = B e^{\frac{y}{L_p}} + B' e^{-\frac{y}{L_p}} \quad (s14b)$$

With  $L_{n(p)} = \sqrt{D_{n(p)} \tau_r}$  the diffusion length of electrons(holes). Using the Eqs. s4(a) and s4(b), we can write the particle flux as follow

$$P_{ny} = -\frac{n\mu}{e} \left( -e\mu B \frac{\partial V_{gr}}{\partial x} + \frac{eD_n}{n_{eq}\mu} \frac{\partial n}{\partial y} \right) \quad (s15a)$$

$$P_{py} = \frac{p\mu}{e} \left( e\mu B \frac{\partial V_{gr}}{\partial x} - \frac{eD_p}{p_{eq}\mu} \frac{\partial p}{\partial y} \right) \quad (s15b)$$

Using the Eqs. s14(a), s14(b), s15(a) and s15(b) combined with the fact the carrier fluxes cancel at the edges of the Hall bar we can show after some calculations that the electron and hole doping write

$$n = n_{eq} + \frac{n_{eq}\mu^2 L_n}{D_n} B \frac{\partial V_{gr}}{\partial x} \frac{sh\left(\frac{y}{L_n}\right)}{ch\left(\frac{W}{2L_n}\right)} \quad (s16a)$$

$$p = p_{eq} + \frac{p_{eq}\mu^2 L_p}{D_p} B \frac{\partial V_{gr}}{\partial x} \frac{sh\left(\frac{y}{L_p}\right)}{ch\left(\frac{W}{2L_p}\right)} \quad (s16b)$$

### III) Longitudinal profile of $V_{gr}$ , $n$ and $p$ for the $1 \mu\text{m}$ wide Hall bar

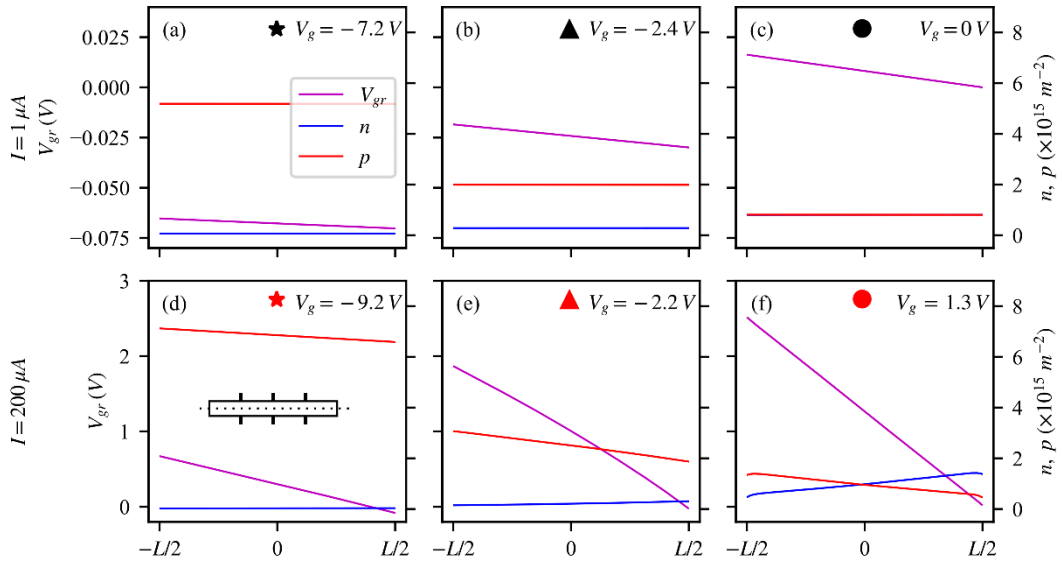


FIG. S3. Charge carrier doping  $n$  (blue curves) and  $p$  (red curves), electrostatic potential  $V_{gr}$  (violet curves) along  $x$  for  $y = 0 \mu\text{m}$  for the  $1 \mu\text{m}$  width Hall bar at three different gate voltage values (see star, triangular and circular symbols on figure 3) and for two bias current values,  $1 \mu\text{A}$  (a), (b), (c) and  $200 \mu\text{A}$  (d), (e), (f). Insert Fig. S1(d): location of the profiles on the Hall bar.

### IV) AFM images of the GHS

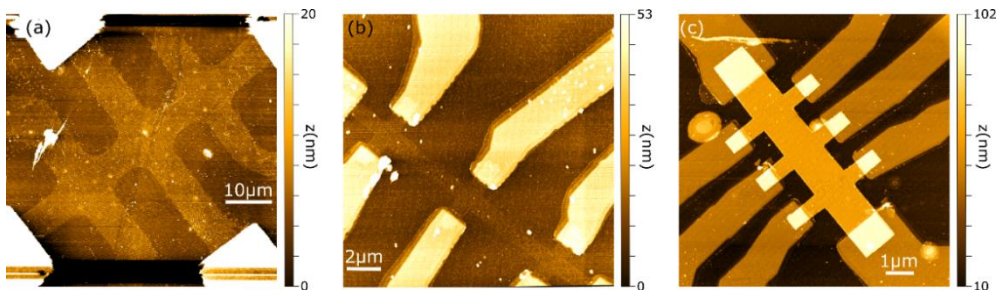


FIG. S4. (a), (b) and (c) AFM image of the CVD-GHS, HOPG-GHS and hBN-GHS respectively. The scratch observed in the middle of the image was made during the observation and after the electrical characterization. The images were obtained with a CSI Nano-Observer in resonant mode using a tip with a stiffness constant equal to  $1.6 \text{ N/m}$ .

## V) CVD electrical characteristics

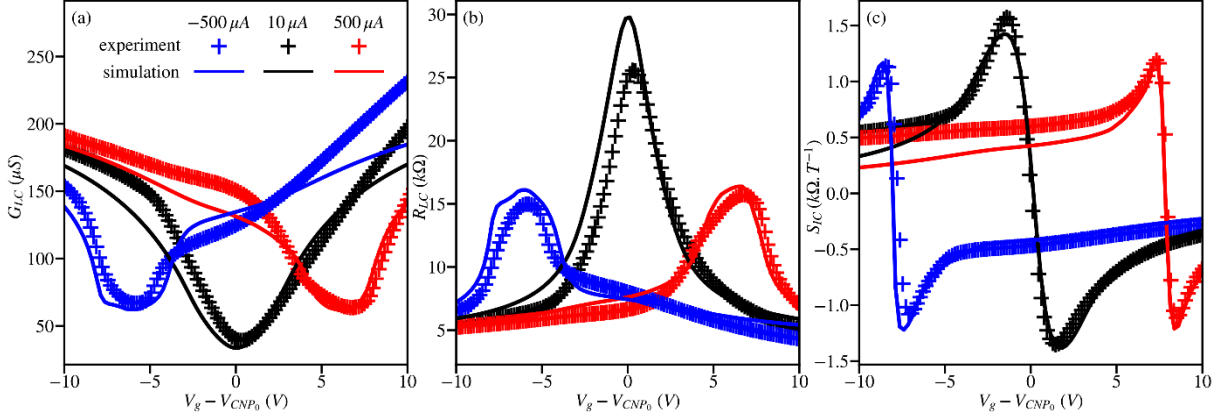


FIG. S5. Experimental (cross) and simulated (line) longitudinal conductance  $G_L$  (a), resistance  $R_L$  (b) and magnetic field sensitivity  $S_I$  (c) of the CVD GHS at three different bias current,  $-500 \mu A$  (blue curves),  $10 \mu A$  (black curves) and  $500 \mu A$  (red curves) performed at 200 K and 1 T.

## VII) Performance degradation with width decrease

Simulations were performed on pristine (without puddles) HOPG-GHS having  $W = 2 \mu m$ ,  $W = 1 \mu m$ ,  $W = 0.5 \mu m$  and  $W = 0.25 \mu m$  at  $T = 300 K$  and  $B = 0.1 T$ . The other dimensions are  $W_h = W$ ,  $W' = 2W$  and  $L = 8W + 3W_h$ . We used for the simulations parameters comparable to what is obtained experimentally:  $\mu = 2 m^2/(V.s)$ ,  $v_f = 1.2 \times 10^6 m/s$  and  $k = 10^{-4} m^2/(V.s)$ . We used for the oxide thickness  $t_{ox} = 280 nm$ .

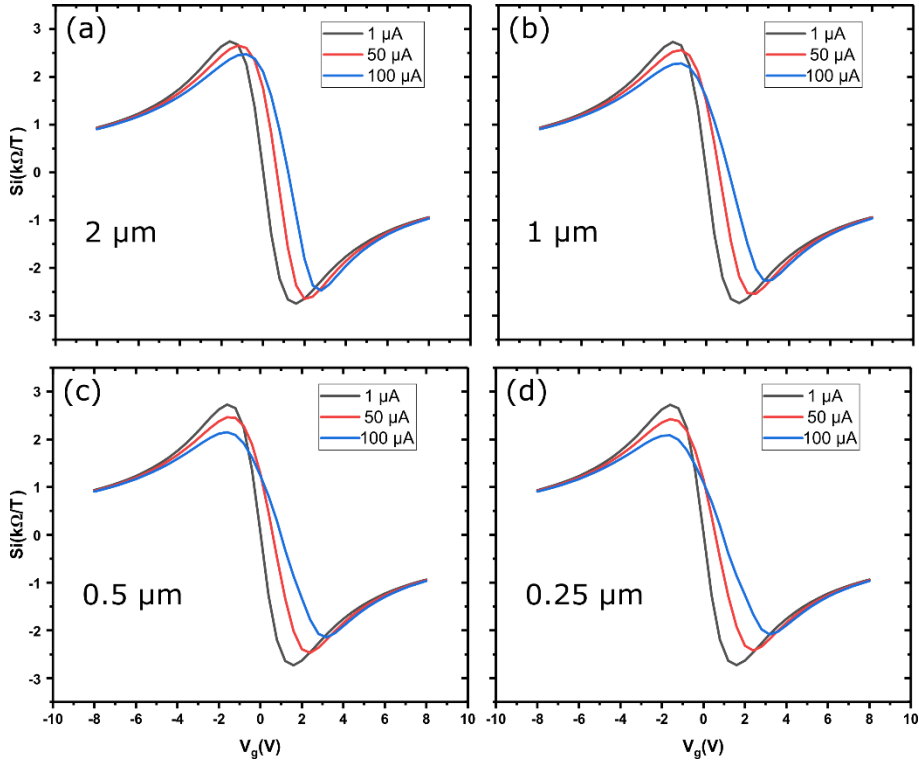


FIG. S6. (a), (b), (c) and (d) Magnetic field sensitivity of a pristine HOPG-GHS with 4 different widths.

We observe that the magnetic field sensitivity degrades (the maximum decreases and the distance separating the extrema increases) when the current increases and the width decreases. This effect is due to a more pronounced effect of the accumulation and depletion areas as the carrier diffusion length is  $740 nm$ .